Geochimica et Cosmochimica Acta 398 (2025) 54–66

Contents lists available at ScienceDirect

Geochimica et Cosmochimica Acta

journal homepage: www.elsevier.com/locate/gca

The effect of CO_2 on the partitioning of H_2O between clinopyroxene and melts and melting of volatile-bearing eclogites

Andrea Curtolo [a,*], Pierre Condamine [b], Federica Schiavi [b], Nathalie Bolfan-Casanova [b], Davide Novella [a]

[a] Dipartimento di Geoscienze, Università degli Studi di Padova, Via Giovanni Gradenigo 6, 35131 Padova, Italy
[b] Laboratoire Magmas et Volcans, CNRS-IRD-OPGC, Université Clermont Auvergne, 6 Avenue Blaise Pascal, 63170 Clermont-Ferrand, France

ARTICLE INFO

Associate editor: Olivier Namur

Keywords:
Eclogite
Mantle
H_2O
Partitioning
CO_2
HIMU

ABSTRACT

H_2O and CO_2 are critical components for the development and sustainment of life on Earth and affect a wide variety of geological processes. It has been suggested that the presence of CO_2 in the mantle could alter how H_2O is stored and partitioned between minerals and melts, implying dramatic effects on both melting processes and H_2O storage capacities of the Earth's mantle. Eclogites, which are present as heterogeneities in the mantle, have been shown to participate in the production of oceanic island basalts such as the HIMU (High-μ, $\mu = {}^{238}U/{}^{204}Pb$). They can host significant amounts of H_2O in clinopyroxenes and their H_2O storage capacity and melting temperature can be significantly influenced by the presence of CO_2. Here, the effect of CO_2 on the partition coefficient of H_2O between clinopyroxene and melt ($D_{H_2O}^{cpx/melt} = C_{H_2O}^{cpx}/C_{H_2O}^{melt}$) was explored at high-pressure and high-temperature by conducting piston cylinder experiments at 1200 °C and 2 GPa. The experiments employed a basaltic starting mixture with different concentrations of H_2O and CO_2 and produced an assemblage consisting of more than 60 wt% basaltic-andesitic melt in equilibrium with high-Al ($Al_2O_3 = 7.83–11.18$ wt%) clinopyroxene crystals. The H_2O concentration in clinopyroxene, measured by Fourier Transform Infrared spectroscopy, ranges from 869 ± 71 to 1950 ± 134 ppm wt, and shows a negative correlation with the concentration of CO_2 in the system and a positive correlation with tetrahedrally-coordinated Al^{3+} in the clinopyroxene. The quenched melts have H_2O and CO_2 concentrations ranging from 5.18 to 6.97 wt% and from 0.19 to 2.59 wt%, respectively. The calculated $D_{H_2O}^{cpx/melt}$ varies from 0.031 ± 0.005 at $XCO_2 = 0.03$ to 0.017 ± 0.003 at $XCO_2 = 0.34$ (where $XCO_2 = CO_2/[H_2O + CO_2]$ in wt). The variation of $D_{H_2O}^{cpx/melt}$ as a function of XCO_2 is described by a power law in the form: $D_{H_2O}^{cpx/melt} = 0.0123 * XCO_2^{-0.237}$, with an extrapolated $D_{H_2O}^{cpx/melt}$ of 0.033 at $XCO_2 = 0$. The calculated $D_{H_2O}^{cpx/melt}$ is combined with $D_{H_2O}^{grt/cpx}$ to constrain the effect of CO_2 on the H_2O partition coefficient between an eclogite and a melt ($D_{H_2O}^{eclo/melt}$), which is then used to predict the melting temperature of eclogite in a hydrous-carbonated system. The results show that melting of hydrous-carbonated eclogite (600 ppm wt H_2O-300 ppm wt CO_2) occurs at temperatures drastically lower than those of both purely hydrous and purely carbonated melting. In this scenario, the temperature of hydrous carbonated melting of eclogite remains lower than the mantle adiabat and crosses the geotherm of the hottest subduction zones at P > 5.8 GPa, indicating that the oceanic crust in a subducting slab could undergo partial melting at this pressure. In addition, $D_{H_2O}^{eclo/melt}$ is used in a simple mass balance model to constrain the H_2O content of a mantle source lithology of HIMU melts, suggested to be made mainly of recycled oceanic crust. The model, using $D_{H_2O}^{eclo/melt}$ at XCO_2 values of 0, 0.1 and 0.3, indicates that partial melting of eclogite with a bulk H_2O content ranging from ~300 to ~720 ppm wt can potentially explain the H_2O abundance measured in magmas originating from the HIMU mantle reservoir.

* Corresponding author.
E-mail address: andrea.curtolo.2@phd.unipd.it (A. Curtolo).

https://doi.org/10.1016/j.gca.2025.03.013
Received 22 July 2024; Accepted 12 March 2025
Available online 16 March 2025
0016-7037/© 2025 The Authors. Published by Elsevier Ltd. This is an open access article under the CC BY license (http://creativecommons.org/licenses/by/4.0/).

1. Introduction

Volatiles (mainly H_2O and CO_2) are present in the Earth's interior as evidenced by their high concentrations in volcanic gases as well as in basaltic lavas that form in the mantle and erupt at mid-ocean ridges or in ocean islands settings (see DeVitre et al., 2023; Fischer et al., 2019; Peslier et al., 2017; van Gerve et al., 2024). Water is the most abundant volatile in both the convective (290 ± 80 ppm wt) and lithospheric (500 ± 150 ppm wt) mantle (Hirschmann, 2018), where it is stored as H impurities in the lattice of nominally anhydrous minerals (NAMs) such as olivine, orthopyroxene, clinopyroxene and garnet (Beran & Libowitzky, 2006; Skogby, 2006). Even in trace concentrations (ppm wt), H_2O strongly influences many physico-chemical properties of minerals including viscosity, electrical conductivity, elastic waves propagation velocity and diffusivity of elements (see e.g., Bolfan-Casanova, 2005; Jacobsen, 2006; Kohlstedt, 2006). Another important effect of H_2O is lowering the melting point of mantle rocks (Green, 1973), which leads to the production of silicate melts at much lower temperatures, at a given pressure, with respect to dry conditions. Melting is therefore facilitated by H_2O in the mantle and occurs over a broader P-T interval than under dry conditions. Given the major role of volatiles such as H_2O in the chemical differentiation of the mantle and in controlling its physico-chemical evolution, understanding and constraining volatile-induced melting processes in the mantle is of critical importance.

Dehydration melting (i.e. melting induced by the presence of H_2O) is triggered in the mantle when the H_2O concentration surpasses the storage capacity of minerals (Hirschmann et al., 2009). The extent of the melting point depression of a rock due to the presence of H_2O is proportional to the concentration of H_2O in near solidus melts in equilibrium with the nominally anhydrous rock (Hirschmann et al., 2009), which in turn is a function of the bulk rock H_2O concentration and the mineral-melt partition coefficients ($D_{H_2O}^{min/melt} = C_{H_2O}^{min}/C_{H_2O}^{melt}$). Therefore, hydrous melting processes in the mantle can be constrained if $D_{H_2O}^{min/melt}$ of different minerals is known at pressures and temperatures representative of the considered mantle environment. These partition coefficients can be determined by performing experiments at high pressures and temperatures (HP-HT) in different chemical systems, which can be challenging given that quenching melts into homogeneous glasses and growing large crystals is difficult, especially at pressures above 3 GPa (e.g., Adam et al., 2016; Myhill et al., 2017; Novella et al., 2017; Novella & Frost, 2014; Sokol et al., 2013; Tenner et al., 2009). Despite these difficulties, precise values of $D_{H_2O}^{min/melt}$ have been determined for the major upper mantle NAMs in both peridotitic and basaltic systems up to 6 GPa (Adam et al., 2016; Aubaud et al., 2004, 2008; Hauri et al., 2006; Koga et al., 2003; Novella et al., 2014; O'Leary et al., 2010; Tenner et al., 2009) providing quantitative constraints of hydrous melting processes in the upper mantle.

Although considerable progress has been made in understanding H_2O partitioning in hydrous mantle rocks, H_2O is not the only significant volatile in the mantle. In fact, C is the second most abundant volatile element (Hirschmann, 2018) and therefore realistic values of $D_{H_2O}^{min/melt}$, representative for the mantle, need to be determined for a system where CO_2 is considered. The addition of CO_2 to a hydrous system will lower the fugacity of H_2O (f_{H_2O}), and since the concentration of H_2O in a mineral is proportional to f_{H_2O} (Keppler & Bolfan-Casanova, 2006; Kohlstedt et al., 1996), the H_2O content of the minerals is expected to be lower in a CO_2-bearing system, decreasing $D_{H_2O}^{min/melt}$. A decrease in $D_{H_2O}^{min/melt}$ will cause solid phases to accommodate less H_2O and will therefore stabilize hydrous melts at temperatures lower than expected for a CO_2-free system.

Understanding the effect of CO_2 on $D_{H_2O}^{min/melt}$ and the stabilization of hydrous-silicate melts is particularly important in volcanic environments, where H_2O and CO_2 contents >1 wt% have been measured in melts erupted at mid ocean ridges (see e.g., Cartigny et al., 2008; Jambon, 1994; Kingsley & Schilling, 1995; Le Voyer et al., 2017, 2019; Ligi et al., 2005) as well as intraplate volcanoes (see e.g., Cabral et al., 2014; Dixon et al., 1997; Gaillard et al., 2021; Taracsák et al., 2019). A lower $D_{H_2O}^{min/melt}$ would not only imply a depression of the solidus, and therefore production of melt at greater depths, but would also cause NAMs in equilibrium with hydrous-carbonated melts to host less H_2O than they would in a CO_2-free scenario (provided the H_2O content of the melts is the same). This is crucial since the H_2O content of melts erupted at mid ocean ridges or at intraplate volcanoes is used to infer the H_2O content of the rocks that formed these melts and consequently the concentration of H_2O in the mantle. Accurate knowledge of the effect of CO_2 on $D_{H_2O}^{min/melt}$ is therefore paramount to model melting processes and infer the H_2O budget of the mantle.

Several studies have investigated the effect of H_2O and CO_2 on mantle melting processes and the composition of melts (Dasgupta et al., 2007; Dvir & Kessel, 2017; Elazar et al., 2019; Foley et al., 2009; Lara & Dasgupta, 2023; Pintér et al., 2021). Several authors have also investigated the solubility of H_2O in different mantle NAMs as a function of the CO_2 concentration (Baptiste et al., 2015; Guo et al., 2020; Yang et al., 2014). These experiments showed that, as CO_2 is added to a system, the solubility of H_2O in olivine or orthopyroxene in equilibrium with pure H_2O or H_2O-bearing melt rapidly decreases due to a decrease in f_{H_2O}. However, determining the effect of CO_2 on $D_{H_2O}^{min/melt}$ is challenging as the starting composition of experiments can be easily contaminated by CO_2, making any assessment of its effect on $D_{H_2O}^{min/melt}$ difficult to accurately characterize without reliable quantification of CO_2 contents. In fact, even experiments that use nominally CO_2–free starting mixtures showed non-negligible concentrations of CO_2 in the melt after the experiment (up to ~1 wt% in some instances, see e.g., Hauri et al., 2006; O'Leary et al., 2010; Tenner et al., 2012). Moreover, the addition of CO_2 decreases H incorporation into minerals, and this makes precise determinations of H_2O in NAMs more challenging. The effect of CO_2 on the H_2O partition coefficient between a peridotite and melt ($D_{H_2O}^{pdt/melt}$) was estimated based on the similar behavior of H_2O and Ce during melting by Dasgupta et al. (2013). The authors estimated a decrease in $D_{H_2O}^{pdt/melt}$ in carbonated silicate melts compared to hydrous silicate melts. However, as of today, only one study equilibrated olivine with a hydrous-carbonated silicate melt and attempted to constrain the influence of CO_2 on $D_{H_2O}^{ol/melt}$ (Sokol et al., 2013). Sokol et al. (2013) performed HP-HT experiments to equilibrate a peridotitic mineral assemblage with H_2O- and CO_2-bearing melts at 6.4 GPa and 1400 °C and determined the H_2O content of olivine and the melts to calculate $D_{H_2O}^{ol/melt}$ in systems with different CO_2 contents. However, while the authors were able to directly measure the H_2O content of olivine, they could only estimate the H_2O content of the melts by mass balance since the melt produced in their experiments could not be quenched into a homogeneous glass. It follows that the effect of CO_2 on $D_{H_2O}^{min/melt}$ of mantle NAMs has yet to be precisely determined and more work is required to precisely constrain volatile-induced melting processes in the mantle.

In this study piston-cylinder experiments were performed at 2 GPa and 1200 °C to investigate the effect of CO_2 on $D_{H_2O}^{min/melt}$ between a basaltic melt and high-Al clinopyroxene representative of an eclogitic lithology (which is composed of a large amount of omphacitic clinopyroxenes). Pyroxenes (in particular clinopyroxenes) dominate melt generation in both eclogitic and peridotitic sources and are major hosts of H_2O in the upper mantle, playing a key role in controlling mantle H_2O content and hydrous melting processes (see e.g., Mierdel et al., 2007; Skogby, 2006). In addition, eclogites are particularly relevant since they are present as an H_2O-rich (Katayama et al., 2006; Nadeau et al., 1993) lithological heterogeneity in the mantle formed by oceanic crust carried at depth by subducting slabs. Subduction-related environments are also

CO_2-rich due to the high CO_2 budget of oceanic slabs (Dasgupta, 2013; Jarrard, 2003) and are important as they are suggested to be a major component of a variety of geochemical reservoirs (such as HIMU, EM1 and EM2) in the mantle that are sampled by oceanic island basalts. In addition, it is likely that the amounts of CO_2 that is carried by arc melts or OIBs have been largely underestimated (Schiavi et al., 2020; Venugopal et al., 2020), implying that CO_2 could have an even greater importance in these environments compared to what was previously expected.

The experiments produced minerals in equilibrium with a melt that quenched into a glass, which allowed precise determination of the H_2O content of both phases by Fourier Transform Infrared (FTIR) spectroscopy and secondary ion mass spectrometry (SIMS). The experiments used varying H_2O and CO_2 concentrations to systematically investigate the effect of XCO_2 on $D_{H_2O}^{cpx/melt}$, and efforts were made to limit and quantify CO_2 contamination in the starting mixtures. The dependence of $D_{H_2O}^{cpx/melt}$ on XCO_2 is then quantified and models are constructed to discuss melting of mantle eclogites in the presence of H_2O and CO_2 and possible implications in the production of magmas related to melting of recycled oceanic crust such as the HIMU endmember.

2. Material and methods

2.1. Starting mixture and experimental procedure

A basaltic composition (similar to AC74, Aubaud et al., 2008) was used as a starting mixture for the experiments. A volatile-free mixture was initially prepared by mixing high-purity oxides (SiO_2, TiO_2, Al_2O_3), carbonates (Na_2CO_3, K_2CO_3) and synthetic mineral powders ($MgSiO_3$ enstatite and $CaSiO_3$ wollastonite). The powder mixture was ground and mixed under ethanol in an agate mortar and collected in a Pt crucible. The Pt crucible containing the powder was then first heated to 600 °C (with a T rate of 100 °C/h) and subsequently to 1300 °C with a lower T rate (50 °C/h) and kept at 1300 °C for 4 h to ensure complete loss of adsorbed volatiles while avoiding loss of material upon heating. After the 24-hour devolatilization cycle, the mixture was quenched into a glass by partially lowering the crucible in cold water, and ground to powder. The devolatilized powder was then mixed with FeO, added at this stage to prevent oxidation of the Fe^{2+}, and $Al(OH)_3$ and $CaCO_3$ as the source of H_2O and CO_2. The mixture was then ground under ethanol, dried and stored in a vacuum oven at 110 °C to avoid volatile adsorption. A shard of the devolatilized glass was analyzed to confirm the oxide composition and to detect eventual volatile contaminations. Major element analyses of the glass conducted with the electron microprobe (EMPA) revealed a slight deficiency of MgO and excess of SiO_2 (<1.5 wt %) compared with the expected composition, most likely a result of the enstatite powder not being completely pure. The final starting mixture differs from the AC74 composition of Aubaud et al. (2008) in terms of SiO_2 (~1.5 wt% excess) and MgO (~1.5 wt% deficiency). Following this procedure, five starting mixtures were prepared with different amounts of H_2O and CO_2 (H_2O-CO_2 in wt% = 6–0; 5–0; 5–0.5; 5–1; 4–2, see Table 1). The compositions reported in Table 1 are calculated based on the weighed proportions of devolatilized mixture (analyzed with EPMA), FeO, $Al(OH)_3$ and $CaCO_3$ to account for the SiO_2 excess and MgO deficiency, while the H_2O and CO_2 contents are those measured by elemental analyzer (see below). Note that the H_2O and CO_2 contents are within 0.25 wt% of the target values.

Synthesis experiments were conducted in a half-inch end-loaded piston cylinder apparatus (Voggenreiter MaVo press LPC 250–300/50) at 2 GPa and 1200 °C at the Laboratoire Magmas et Volcans (LMV, Université Clermont Auvergne, Clermont-Ferrand, France). The assemblies consisted of a NaCl cell wrapped in a Teflon sheet, a Pyrex tube, a straight graphite heater and spacers of crushable MgO. A $Au_{80}Pd_{20}$ capsule was used to minimize H_2O loss during the experiment. The temperature was monitored during the experiment with a type C thermocouple and was kept within 1 °C of the target temperature using a Eurotherm temperature controller. To ensure complete melting and promote crystal growth, the experiments were first heated to 1350 °C for 30 min and then slowly cooled (at a rate of 50 °C/h) to the target temperature of 1200 °C where they were held for 6 h. Experiments were stopped and quenched by shutting off the power supply to the apparatus.

Table 1
Composition of starting mixtures (wt% oxides).

Run no.	B6-0	B5-0	B5-0.5	B5-1	B4-2	AC74[c]
SiO_2	48.62	49.14	48.88	48.62	48.62	47.54
TiO_2	1.70	1.72	1.71	1.70	1.70	1.48
Al_2O_3	14.89	15.05	14.97	14.89	14.89	15.14
FeO	9.38	9.48	9.43	9.38	9.38	8.86
MgO	6.31	6.37	6.34	6.31	6.31	7.93
CaO	10.09	10.20	10.14	10.09	10.09	9.99
Na_2O	2.85	2.88	2.87	2.85	2.85	2.84
K_2O	0.16	0.16	0.16	0.16	0.16	0.20
H_2O[a]	6.09(18)	5.22(4)	5.22(9)	5.23	4.18(12)	6.00
CO_2[a]	0.19(2)	0.14(1)	0.75(2)	1.16	2.17(3)	–
XCO_2[b]	0.03	0.03	0.13	0.18	0.34	–
Tot	100.28	100.36	100.47	100.39	100.35	100.00

[a] Concentrations measured using a CHNS elemental analyzer; error between brackets is 1SD based on 2–3 analyses.
[b] XCO_2 is calculated as $XCO_2 = [CO_2/(H_2O + CO_2)]$ using the concentrations of H_2O and CO_2 reported in this table. Errors for XCO_2 calculated from error propagation of the SDs reported for H_2O and CO_2 always results <0.01 and is therefore omitted.
[c] Composition of AC74 reported by Aubaud et al. (2008), normalized to 100 after removing Cr_2O_3 and MnO and adding 6 wt% H_2O.

2.2. Analytical techniques

2.2.1. CHNS/O Elemental Analyzer

Analyses of the H_2O and CO_2 concentration of the starting mixture that were used in the experiments were performed with a Thermo Scientific Flash 2000 CHNS/O Elemental Analyzer at LMV. Approximately 1 mg of powder was weighed and burned in a 950 °C furnace with He used as a carrier gas. The volatiles were then separated by chromatography and quantified with a thermal conductivity universal detector by comparison with synthetic standards. The volatile content of each starting mixture is reported in Table 1.

2.2.2. EPMA

The quenched experiments produced clinopyroxene crystals in equilibrium with large pools of glass (Fig. 1). After every experiment the capsule was cut in half. One half was embedded in epoxy resin and

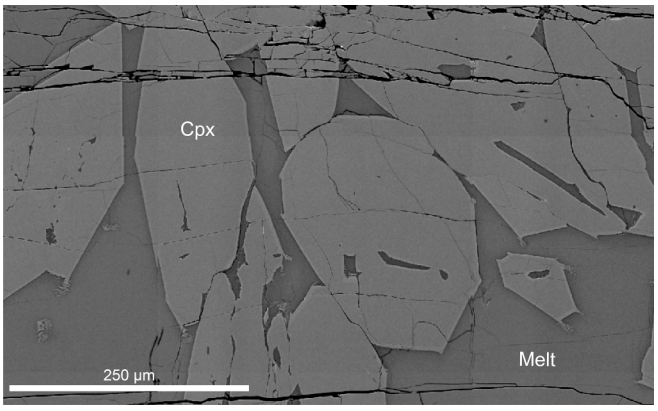

Fig. 1. Backscattered electron image of experimental charge (run B5-1). Large clinopyroxene crystals (light grey) are immersed in a homogeneous melt pool (dark grey). Cracks are the result of the rapid decompression of the sample at the end of the piston-cylinder experiment.

polished with a final suspension of diamonds 0.25 μm in size. The sample mount was then C-coated and major element concentrations of minerals and melts were determined using a Cameca SXFive-TACTIS electron microprobe at LMV. The standards used for the analyses are wollastonite (Si and Ca), orthoclase (Al and K), albite (Na), forsterite (Mg), fayalite (Fe), Cr_2O_3 (Cr), NiO (Ni), and $MnTiO_3$ (Mn and Ti). Crystals of clinopyroxene were analyzed with a focused beam of ~1 μm employing a 15 kV voltage and a 15 nA current with counting times of 10 s. For glasses, a defocused 8 nA beam with a size of 20 μm was used in the analyses. The samples were analyzed avoiding cracks, and at least 10 analyses were performed on each phase in every sample. Glass and mineral compositions were used together with the bulk composition of the starting mixture to calculate the proportion of each phase in the charges by mass balance calculations. From the mass balance calculations, no Fe-loss caused by alloying to the capsule was observed. The composition of the phases and their proportions in each experiment are reported in Table 2.

2.2.3. FTIR spectroscopy

The H_2O and CO_2 content of synthesized glasses and clinopyroxenes was determined by FTIR spectroscopy using a Bruker Vertex 70 spectrometer coupled with a Hyperion microscope at LMV. Half capsules that were recovered after the experiments were double polished to 100–150 μm to perform absorption analyses. Sample thicknesses were measured with a Mitutoyo digital caliper with an accuracy of ±5 μm or using the laser beam focusing of the Raman micro-spectrometer as described in Schiavi et al. (2018), with an accuracy of ±1 μm. Spectra were collected through a CaF_2 window with 100 and 300 scans for background and sample, respectively, and a spectral resolution of 2 cm^{-1}.

Glasses were analyzed using unpolarized radiation and a variable beam size depending on the sample, with an area of approximately 100 x 100 μm. The analyses were carried out on melt pools avoiding cracks, and concentrations of OH^- and molecular H_2O were determined using the integrated absorbances of the bands at 4500 and 5200 cm^{-1} (Ohlhorst et al., 2001). Approximately 10 spectra were collected for the glass phase in each experiment. For H_2O quantification, the baselines were determined by manually fitting two gaussians at ~5400–5500 and ~4000 cm^{-1} as indicated by Ohlhorst et al. (2001). Absorption coefficients were calculated based on the SiO_2 content of the glasses (volatile-free and normalized to 100 wt%) following the equation in Ohlhorst et al. (2001). For CO_2 quantification, the baselines were taken as cubic splines around the region at 1400–1500 cm^{-1}, and the absorption coefficient of Fine & Stolper (1985) was used. CO_2 quantification was possible only on nominally C-free experiments, since in C-bearing glasses the bands saturate the spectra (Fig. S1). Densities of the glasses were calculated as a function of the total H_2O content with the formula for Fe-rich basalts following Schiavi et al. (2018). An iterative approach was followed: (i) a placeholder density was used to calculate the total H_2O concentration; (ii) the total H_2O concentration calculated in (i) was used to calculate a density; (iii) the density was calculated for the H_2O content calculated in (ii), and this process was repeated until convergence. This procedure resulted in errors (calculated as the standard deviation of multiple analyses) mostly <10 %.

Extracting crystals from the experimental capsules and orienting them according to their optical axes to perform polarized analyses is very complex given their small size and monoclinic symmetry, which implies that only one optical axis coincides with a crystallographic axis. Unoriented analyses on an anisotropic phase can result in errors in the quantification of H_2O due to the measurement of projections on a random surface of the principal absorbances vectors instead of the principal absorbances themselves (Libowitzky & Rossman, 1996). Therefore, the determination of H_2O in clinopyroxenes used the same acquisition conditions as for the glasses, but a smaller beam size and polarized radiation. To reduce the possible error due to measurement on unoriented anisotropic samples, polarized measurements were collected rotating the polarizer by 180° with acquisitions approximately every 10°. This approach was followed to measure as many different orientations of the optical vectors as possible, producing statistically significant H_2O quantifications (with an error that is on average <20 %, see supplementary materials). The baselines of the spectra were taken as cubic splines. The Beer-Lambert law was used to determine clinopyroxene H_2O contents with three different absorption coefficients, two clinopyroxene-specific coefficients (Bell et al., 1995; Koch-Müller et al., 2007) and a general wavenumber-dependent coefficient (Libowitzky & Rossman, 1997). The propagated error for this approach is usually <10 % regardless of the coefficient used for the calculation. However, given the considerations regarding measurements on unoriented samples above, and the statistical calculations in the supplementary materials, it

Table 2
Composition of minerals and melts (wt% oxides) synthesized in the experiments.

Run no.	B6-0		B5-0		B5-0_4*		B5-0.5		B5-1		B4-2	
Phase	Cpx	Glass	Cpx	Glass	Cpx	Glass	Cpx	Glass	Cpx	Glass	Cpx	Glass
wt%	3	97	33	66	30	70	18	82	20	80	22	78
Res.	0.79		0.23		0.16		0.55		0.15		0.56	
n	11	20	21	18	19	15	55	27	26	20	29	30
SiO_2	50.41	48.75	48.39	49.89	48.51	48.78	49.42	48.92	48.76	48.74	49.48	49.08
	(37)	(28)	(42)	(34)	(47)	(28)	(62)	(40)	(59)	(39)	(51)	(34)
TiO_2	0.46	1.73	0.84	2.13	0.89	2.13	0.64	1.85	0.89	1.90	0.66	1.93
	(6)	(5)	(13)	(10)	(19)	(7)	(14)	(8)	(23)	(10)	(12)	(5)
Al_2O_3	7.83	14.51	11.18	16.67	10.80	16.51	9.64	15.49	10.83	15.77	10.52	15.60
	(38)	(13)	(49)	(21)	(61)	(21)	(83)	(25)	(42)	(27)	(16)	(16)
FeO_t	6.96	9.69	8.99	9.36	8.73	9.86	7.98	9.43	8.56	9.02	8.82	9.58
	(14)	(18)	(25)	(16)	(43)	(10)	(31)	(13)	(27)	(19)	(26)	(14)
MgO	13.41	6.01	11.42	4.47	11.69	4.57	12.57	5.24	11.91	4.98	12.41	4.96
	(23)	(9)	(34)	(9)	(40)	(22)	(50)	(11)	(42)	(17)	(34)	(19)
CaO	19.77	9.53	16.93	7.27	17.37	7.46	17.89	8.50	17.41	8.33	16.49	8.39
	(22)	(9)	(35)	(10)	(32)	(28)	(35)	(9)	(41)	(14)	(44)	(20)
Na_2O	1.32	2.96	1.80	3.46	1.68	3.36	1.51	3.10	1.63	3.12	1.64	3.06
	(4)	(6)	(11)	(8)	(9)	(16)	(9)	(8)	(8)	(12)	(7)	(10)
K_2O	BD	0.15	BD	0.30	BD	0.30	BD	0.21	BD	0.21	BD	0.23
		(1)		(1)		(3)		(2)		(2)		(2)
Tot	100.16	93.33	99.55	93.55	99.67	92.97	99.65	92.74	99.99	92.10	100.02	92.83
K_D^{Fe-Mg}	0.32		0.38		0.35		0.35		0.40		0.37	

BD = below detection limit; error between brackets is 1SD based on multiple analyses; "wt%" indicates the weight proportion of the phases obtained from mass balance calculations. "Res." refers to residuals from the mass balance calculations.

* B5-0_4 is a repetition of the experiment performed with starting mixture B5-0.

is possible for the real error to be different. Average FTIR spectra for the H_2O vibration regions of clinopyroxenes and melts are shown in Fig. 2.

2.2.4. SIMS

In addition to FTIR analyses, SIMS was employed to measure the CO_2 content of glasses (to detect possible C contamination). This was done because in all CO_2-bearing systems the FTIR signal related to $(CO_3)^{2-}$ vibrations (see section 3.2) was saturated (see Fig. S1). Moreover, the H_2O contents of both minerals and melts were analyzed. Hydrogen and carbon abundances in the phases were measured with a CAMECA IMS1280-HR2 SIMS at the Centre de Recherches Pétrographiques et Géochimiques (CRPG, Université de Lorraine, Nancy, France), which used a 20 keV Cs^+ primary beam and a <5 x 10^{-9} mbar vacuum in the analytical chamber. Prior to the analyses, sample mounts were pre-sputtered at a current of 1nA with a raster size of 7 x 7 μm to clean the surface of any adsorbed H, and then a beam with a current of 1nA was used for the analyses with a raster size of 5 x 5 μm. The reference materials used as standards for the analyses are described in Peslier et al. (2002) and Mosenfelder & Rossman (2013). The error in these quantifications (calculated as 1SD based on multiple analyses) is generally <5 %. For clinopyroxenes, a linear calibration of ppm wt H_2O vs OH/Si*SiO_2 was employed (Fig. S2) while a second-degree polynomial of H_2O/SiO_2 vs OH/Si was used for the calibration of the melts (Fig. S3), as suggested by Koga et al. (2003).

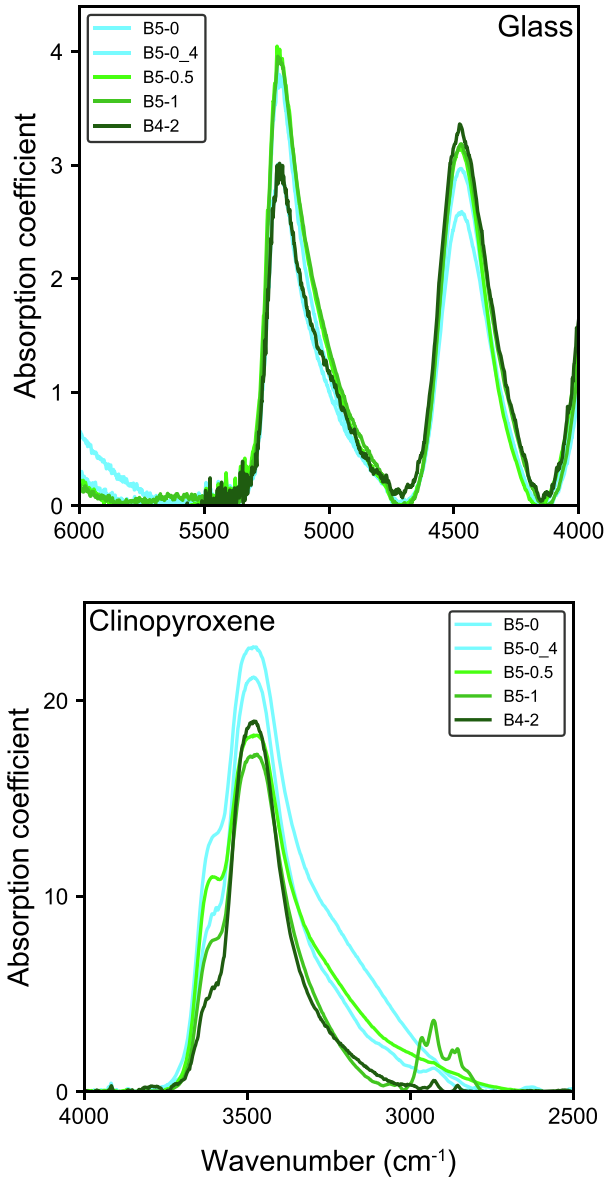

Fig. 2. Average FTIR spectra (normalized to a sample thickness of 1 cm) of the water vibration region of silicate glasses and clinopyroxene for each experimental run in this study. Spectra B5-0 and B5-0_4 (both in light blue) represent two different runs that employed the same starting mixtures (indicated as B5-0 in Table 1) and where partial water-loss was recorded in one of them (run B5-0). The small signal between 2700 and 3000 cm^{-1} in run B5-1 is caused by the epoxy resin used during the sample preparation. Experiment B6-0 is not represented here as its low clinopyroxene $^{IV}Al^{3+}$ causes it to have the lowest clinopyroxene H_2O concentration.

2.2.5. Raman spectroscopy

Raman spectroscopy was used to quantify CO_2 concentration in the glasses. Measurements were performed with a Renishaw inVia confocal Raman micro-spectrometer equipped with a 532 nm diode-pulsed solid-state-laser and a Leica DM 2500 M microscope at LMV. The samples have been measured with a grating of 2400 grooves/mm, a laser power of 3 mW on the sample and 120 s (30 s x 4) of acquisition time. Reference samples and details describing the procedure can be found in Buso et al. (2022). Repeated quantification performed on the same sample allows the error (expressed as 1 SD) to be estimated as being always <5 %.

3. Results

3.1. Phase assemblages and chemical composition of clinopyroxene and melt

Major element equilibrium was achieved during the experiments as indicated by the K_D^{Fe-Mg} (= $[FeO^{cpx}MgO^{melt}]/[FeO^{melt}MgO^{cpx}]$ with all Fe assumed to be present as Fe^{2+}) coefficient, which ranges from 0.32 to 0.40 (Table 2), in agreement with values reported in similar systems (e.g., O'Leary et al., 2010). In addition, very fast diffusion of H in clinopyroxenes (Ingrin & Blanchard, 2006) ensures its equilibration between crystals and melt at the timescales of the experiments.

Mass balance calculations with the inclusion of pure Fe as a theoretical phase indicate no detectable Fe-loss (abundance of pure Fe ~0 wt %) from the starting mixture to the capsule during the HP-HT experiments. Melts are the most abundant phase, comprising 67 to 82 wt% in each experimental run, reaching 97 wt% in experiment B6-0. The melts fall in the low SiO_2 end of the basaltic andesitic series, with a SiO_2 concentration around 53 wt% and a total alkali content ($Na_2O + K_2O$) ranging from ~3 to ~4 wt% on a volatile-free normalized basis (Table 2). The Mg# (=$Mg/[Mg + Fe^{tot}]$) of the silicate melts range from 0.45 to 0.52, and these values are lower than the range given by O'Leary et al. (2010) for similar experiments due to the deficiency of MgO in the starting mixture used here. Minor compositional trends are observed as a function of the melt fraction in the experiment calculated using a mass balance, with progressive enrichment in MgO and CaO and depletion in SiO_2, Al_2O_3, TiO_2 and Na_2O as the melt fraction increases (Fig. S4).

Clinopyroxenes generally formed elongated crystals, typically >50 μm long. Their abundance varies between 18 and 33 wt% (except for sample B6-0 with only 3 wt% clinopyroxene) following mass balance calculations. The compositions of clinopyroxenes crystallized in this study are similar to those reported for clinopyroxenes during partial melting of eclogite (see e.g., Pertermann & Hirschmann, 2003; Yasuda et al., 1994). The clinopyroxenes have a Mg# between 0.69 and 0.77 and high Al^{3+} in tetrahedral coordination ($^{IV}Al^{3+} = 2 - Si = 0.15$ to 0.21; Table S1). A progressive enrichment in $^{IV}Al^{3+}$ is observed with decreasing melt fraction (Fig. S5), with the lowest value of $^{IV}Al^{3+}$ belonging to the sample with the highest melt abundance (B6-0). The end member compositions of clinopyroxene in this study are: 9–13 % jadeite [$NaAlSi_2O_6$], 50–69 % diopside-hedembergite [$Ca(Mg,Fe)Si_2O_6$], 13–23 % enstatite-ferrosilite [$(Mg,Fe)_2Si_2O_6$] and 9–15 % Ca-tschermakite [$CaAl(Si,Al)_2O_6$].

3.2. Volatile concentrations

The H_2O content of silicate melts measured using FTIR ranges from 5.18 to 6.97 wt% (Table 3) and is in good agreement with values measured using SIMS (within 15 % relative) that range from 5.27 to 6.77 wt% (Table S2). The largest discrepancy between the two techniques is observed at lower H_2O contents (Fig. S6), while at high H_2O concentrations the two independent quantifications show better agreement. Interestingly, SIMS measurements provide higher H_2O concentrations for all (nominally) CO_2-free samples and lower H_2O concentrations for CO_2-bearing experiments, with respect to FTIR values. Using the 4500 and 5200 cm^{-1} IR bands, the speciation of water into molecular H_2O and OH^- groups in the melts was determined (Fig. 3). The concentration of molecular H_2O ranges from 2.97 to 4.12 wt%, while the OH^- concentration ranges from 2.22 to 2.89 wt% (Table 3), in agreement with basaltic samples with similar total water content reported by Ohlhorst et al. (2001).

The CO_2 concentration in the silicate melts ranges from 0.18 to 2.59 wt% as determined by SIMS analyses (Table S2); these results are consistent with CO_2 contents determined by FTIR for nominally CO_2-free samples ranging between 0.11 and 0.17 wt% CO_2 and with values measured by Raman spectroscopy for CO_2-bearing samples ranging from 1.04 to 2.11 wt% CO_2 (see discussion below, Table S2 and Fig. S7). These CO_2 concentrations in the melts indicate that the sample was not contaminated by the assembly (the graphite furnace) during the experiment. FTIR spectra show absorption bands around ~1430 and ~1520 cm^{-1}, and no signal at ~2350 cm^{-1} is observed, indicating that all the C is stored in the melt in the form of $(CO_3)^{2-}$ groups, as expected for basic compositions (Ni & Keppler, 2013).

Three different integrated absorption coefficients were used to calculate the H_2O concentration in the clinopyroxenes in this study (Bell et al., 1995; Koch-Müller et al., 2007; Libowitzky & Rossman, 1997), providing different results (Table 3). Among the three calibrations, the lowest H_2O concentrations are calculated using the calibration of Libowitzky & Rossman (1997), with values ranging from 790 ± 49 to 1443 ± 104 ppm wt H_2O. The calibration from Bell et al. (1995) provides the highest concentrations (1475 ± 120 to 3310 ± 227 ppm wt H_2O) while the more recent coefficient determined by Koch-Müller et al. (2007) provides concentrations of 869 ± 71 to 1950 ± 134 ppm wt H_2O.

Water contents measured with SIMS range from 1175 ± 94 to 1637 ± 74 ppm wt H_2O and show the best agreement with FTIR when using the coefficient of Koch-Müller et al. (2007) (Table S3). The absorption coefficient of Koch-Müller et al. (2007) is used in subsequent discussions because of its good agreement with SIMS measurement and its calibration on omphacitic clinopyroxenes with a composition similar to those in this study. Clinopyroxenes in experiment B5-1 also show minor absorption bands between ~2750 and ~3000 cm^{-1} due to some contamination of the sample by the epoxy resin used during the sample preparation (Fig. 2). This contamination has, however, no impact on the calculated H_2O content of the clinopyroxenes as only the signal in the OH stretching region at higher wave numbers is used to determine the H_2O content for those particular samples.

The H_2O concentration of clinopyroxenes and melts were combined with the phase abundances obtained from mass balance calculations of the major and minor oxides and used to calculate the H_2O concentration of the bulk of each experiment. These calculations show that experiment B5-0 experienced partial H_2O-loss, resulting in a calculated initial H_2O concentration more than 1 wt% lower than the actual concentration measured on the starting mixture with the CHNS elemental analyzer (Table S4).

Table 3
H_2O concentration in synthesized phases and mineral/melts partition coefficients from FTIR analyses.

	H_2O cpx (ppm wt)			H_2O melt (wt%)			
Run no.	**B95**	**LR97**	**KM07**	**OH^-**	**H_2O_m**	**H_2O_{tot}**	**$D_{H_2O}^{cpx/melt}$**
B6-0	1475	790	869	2.48	3.16	5.64	0.015
	(120)	(49)	(71)	(9)	(22)	(22)	(1)
B5-0	2444	1204	1459	2.22	2.97	5.18	0.028
	(269)	(124)	(159)	(23)	(27)	(46)	(4)
B5-0_4	3310	1443	1950	2.52	3.80	6.32	0.031
	(227)	(104)	(134)	(31)	(61)	(83)	(5)
B5-0.5	2528	1197	1490	2.56	4.10	6.66	0.022
	(130)	(55)	(77)	(7)	(12)	(16)	(1)
B5-1	1830	963	1078	2.85	4.12	6.97	0.015
	(103)	(48)	(61)	(34)	(28)	(58)	(2)
B4-2	1722	890	1015	2.89	3.07	5.96	0.017
	(195)	(95)	(115)	(85)	(47)	(63)	(3)

Error between brackets is 1SD calculated by error propagation in clinopyroxene and based on multiple analyses on melts. $D_{H_2O}^{cpx/melt}$ was calculated using the concentration of H_2O in clinopyroxene measured using the KM07 calibration (Koch-Müller et al., 2007) and the total H_2O content in the glass (H_2O_{tot}). Error for $D_{H_2O}^{cpx/melt}$ was calculated by error propagation from the errors of the clinopyroxene and melts.

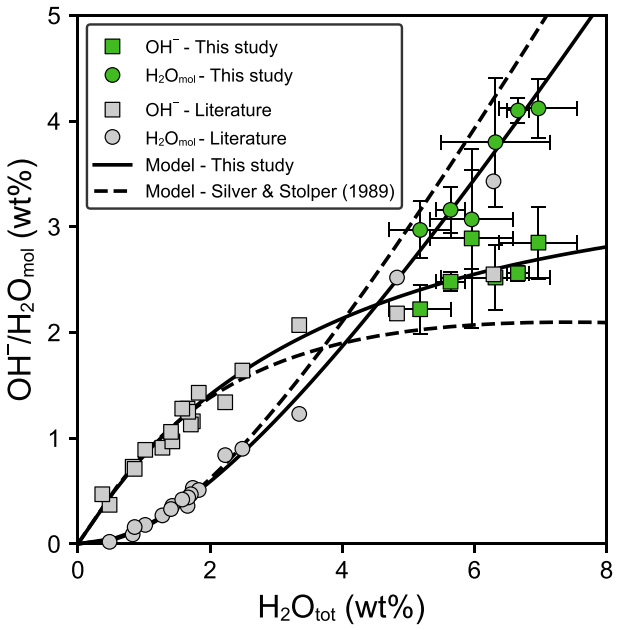

Fig. 3. Concentration of molecular H_2O and OH^- in silicate melts as a function of the total H_2O content. Data listed as "- Literature" in the legend are from basalts measured by Dixon et al. (1995) and Ohlhorst et al. (2001). The dashed lines represent the concentration of OH^- and molecular H_2O calculated using the water speciation model described by Eq. (5) of Silver & Stolper (1989) and their calibration. The solid lines represent the recalibration done in this study of the Silver & Stolper (1989) model using data from Dixon et al. (1995), Ohlhorst et al. (2001) and this study.

4. Discussion

The H_2O concentrations in melts and clinopyroxenes measured using FTIR were used for the discussion that follows as the H_2O contents determined by SIMS use extrapolations of the calibration (especially for clinopyroxenes, see Fig. S2), introducing potential uncertainties. This is particularly noticeable in melts, where the choice of a linear or a second-degree polynomial calibration line leads to differences up to ~1 wt% in the final H_2O concentration despite both providing a good fit (R^2 = 0.998 for both) to the standards (Fig. S3).

As demonstrated by previous works, $^{IV}Al^{3+}$ influences the amount of H_2O incorporated in clinopyroxene through the coupled substitution $^{IV}Si^{4+} = {}^{IV}Al^{3+} + H^+$, causing clinopyroxene with a high $^{IV}Al^{3+}$ to incorporate more H_2O (e.g., O'Leary et al., 2010). In experiment B6-0,

clinopyroxene has a $^{IV}Al^{3+}$ content lower than in the other experiments, consistent with the larger degree of melting and also has a lower H_2O concentration. Because of this, the experiment was not considered in the discussion as its low $^{IV}Al^{3+}$ content may overshadow the effects of CO_2 on H_2O incorporation. It is important to note, however, that in clinopyroxene, most of the $^{IV}Al^{3+}$ will be present as a Tschermak-substitution ($^{VI}M^{2+} + {}^{IV}Si^{4+} = {}^{VI}Al^{3+} + {}^{IV}Al^{3+}$, with M^{2+} being a divalent cation), and this will not lead to higher H^+ incorporation, so there might be a different reason for the lower H_2O content of experiment B6-0. All remaining experiments produced clinopyroxene with the same $^{IV}Al^{3+}$ content within error (Table S1), allowing to directly compare the results of each experiment in order to address the effect of CO_2.

The concentration of H_2O in clinopyroxene decreases linearly with increasing XCO_2 (Fig. S8). This negative correlation is observed up to an XCO_2 of ~0.2, after which the H_2O concentration decreases very weakly with increasing XCO_2. A similar behavior was observed by Yang et al. (2014) in HP-HT experiments (1.5 GPa, 1100 °C) where olivine was equilibrated with H_2O and CO_2 bearing fluids. In those experiments, H_2O concentration in olivine was observed to decrease as CO_2 entered the system, but by $XCO_2 > 0.38$ (by weight) it remained constant. This behavior is difficult to constrain as the activity (or fugacity) of volatile components in silicate melts cannot be precisely determined. Nevertheless, some general observations can still be made regarding the behavior of H_2O and its concentration as a function of the CO_2 content focusing on experiments B5-0_4, B5-0.5 and B5-1 where H_2O concentrations were held constant and CO_2 contents were progressively increased. The H_2O content of clinopyroxenes equilibrated in these experiments can be fitted as a function of XCO_2. Extrapolating to $XCO_2 = 0$ indicates a H_2O content of ~2114 ppm wt. Given that a linear fit provides the best interpretation of the H_2O contents (with a $R^2 = 0.983$; Fig. S8), it is implied that the H_2O concentration in clinopyroxene decreases linearly as CO_2 is added to the system, at least up to a certain XCO_2. According to the H_2O solubility law of Kohlstedt et al. (1996) and solubility experiments on clinopyroxenes (Bromiley et al., 2004; Bromiley & Keppler, 2004), the concentration of H_2O in a clinopyroxene should be proportional to $\sqrt{f_{H_2O}}$. It follows that, in order to observe a linear decrease of the H_2O concentration with CO_2, f_{H_2O} must decrease as a second-degree polynomial when CO_2 enters the system, at least up to a certain XCO_2 (=0.2, as observed in this study). On the other hand, the incorporation of H_2O in the silicate melt equilibrated with clinopyroxene does not seem to change dramatically by changing the bulk CO_2 content.

The H_2O concentration measured in clinopyroxene and melt in each experiment allowed calculations of $D_{H_2O}^{cpx/melt}$ as reported in Table 3. The $D_{H_2O}^{cpx/melt}$ calculated in this study are in agreement with the range of values reported in the literature (Adam et al., 2016; Aubaud et al., 2004, 2008; Hauri et al., 2006; Novella et al., 2014; O'Leary et al., 2010; Tenner et al., 2009) at various pressure and temperature conditions (Fig. 4). Agreement with previous data is also observed for the dependence of $D_{H_2O}^{cpx/melt}$ on $^{IV}Al^{3+}$ (Fig. S9), as expected following the results of previous works (e.g., O'Leary et al., 2010).

An effect of CO_2 on $D_{H_2O}^{cpx/melt}$ is clearly noticeable as shown in Fig. 5. Following the H_2O concentration in clinopyroxene, $D_{H_2O}^{cpx/melt}$ decreases as CO_2 is added to the system, up to $XCO_2 = 0.2$, and appears to remain constant at $XCO_2 > 0.2$. The variation of $D_{H_2O}^{cpx/melt}$ with CO_2 is within the range of variability of partition coefficients reported in the literature as a function of pressure, temperature and composition (Fig. 4), implying that the effect of CO_2 is noticeable only when the other parameters are held constant or change slightly. The measured $D_{H_2O}^{cpx/melt}$ were fitted as a function of XCO_2, with the best fit ($R^2 = 0.893$) provided by the following equation:

$$D_{H_2O}^{cpx/melt} = 0.0123 * XCO_2^{-0.237} \quad (1)$$

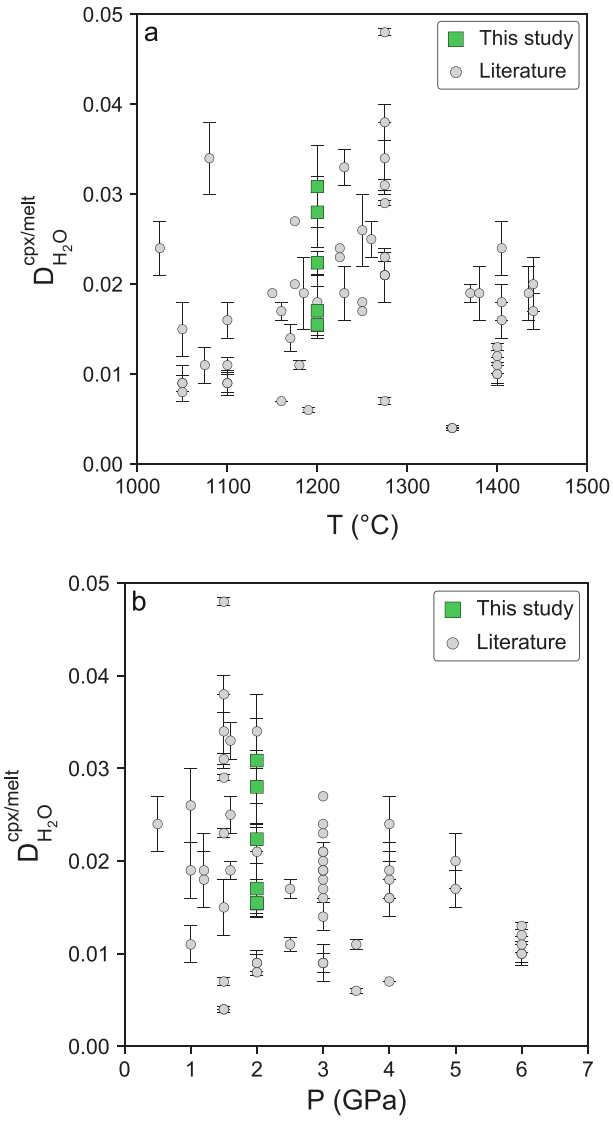

Fig. 4. $D_{H_2O}^{cpx/melt}$ as a function of temperature (a) and pressure (b). Grey circles are data from experiments in the literature (Adam et al., 2016; Aubaud et al., 2004, 2008; Hauri et al., 2006; Novella et al., 2014; O'Leary et al., 2010; Tenner et al., 2009) conducted in compositions ranging from peridotitic to basaltic.

This empirical fit applies only at XCO_2 concentrations between 0 and 0.34 and other intensive variables (including bulk composition as well as P, T and f_{O_2}) close to the experiments described here. Importantly, since Eq. (1) is a negative power law, $D_{H_2O}^{cpx/melt}$ will approach infinity as XCO_2 approaches 0, which is unreasonable. However, a reasonable value of $D_{H_2O}^{cpx/melt}$ in a completely CO_2-free system can be estimated by using the H_2O content of the melt in experiment B5-0_4 (which has an XCO_2 close to 0, at 0.03), and the H_2O concentration in the clinopyroxene estimated for a CO_2-free system (see above). This calculation results in a $D_{H_2O}^{cpx/melt}$ of 0.033 at $XCO_2 = 0$.

The observed behavior of $D_{H_2O}^{cpx/melt}$ with increasing CO_2 is likely due to a decrease of f_{H_2O}, which in turn could be caused by interactions between OH^-, molecular H_2O and $(CO_3)^{2-}$ in the silicate melt. It is well known that OH^- interacts with the melt by breaking Si-O-Si bonds (McMillan, 1994), creating non-bridging oxygens (NBOs) where H bonds forming Si-OH groups (Stolper, 1982). On the other hand, it is known that the abundance of $(CO_3)^{2-}$ groups in silicate melts increases (with respect to CO_2) with increasing abundance of NBOs and that

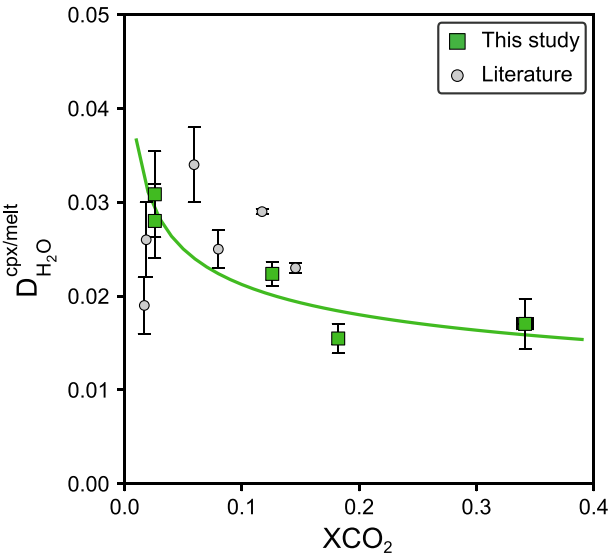

Fig. 5. $D^{cpx/melt}_{H_2O}$ as a function of XCO_2 (=CO_2/[CO_2 + H_2O]) of the system. Experiment B6-0 is not plotted because of its low $^{IV}Al^{3+}$, overshadowing the effect of XCO_2 on $D^{cpx/melt}_{H_2O}$. Grey circles are data from the literature (Aubaud et al., 2004; Hauri et al., 2006; O'Leary et al., 2010) where data regarding the CO_2 concentration in the melt were available together with the phase proportions to calculate XCO_2 of the system, and where $^{IV}Al^{3+}$ of the clinopyroxene was between 0.16 and 0.25 apfu. The solid line is the best fit describing the variation of $D^{cpx/melt}_{H_2O}$ as a function of XCO_2. Differences between data from this work and the literature could be caused by differences in composition, pressure or temperature of the experiments, and the uncertainty on the calculation of XCO_2 for the literature data.

$(CO_3)^{2-}$ is most likely attached to Si cations via NBOs (Ni & Keppler, 2013). It is therefore possible to speculate that some interactions can occur between OH^-, $(CO_3)^{2-}$ and NBOs, possibly forming complexes that promote dissolution of H_2O in the structure of silicate melt rather than into that of clinopyroxene, thus making H_2O more incompatible. This effect may become saturated at some XCO_2 values depending on the composition of the melt (and therefore its structure and NBOs availability) or the mineral species involved. This could explain the different values of XCO_2 after which the H_2O content of minerals seems to remain constant regardless of CO_2 addition observed in this study and Yang et al. (2014). It is important to clarify, however, that as of today very little is known about the structure and energetics of silicate melts with coexisting H_2O and CO_2, and therefore more work is needed before some conclusive hypotheses can be advanced describing their interactions in melts.

4.1. Eclogite melting in the presence of H_2O and CO_2

The $D^{cpx/melt}_{H_2O}$ determined in this study are used to model the melting of eclogitic lithologies in the presence of both H_2O and CO_2. In a scenario where H_2O is the only volatile present in the system, its effect on the depression of the solidus temperature of the rock can be modelled using the cryoscopic equation, where the temperature of the dehydration solidus is calculated as:

$$T = \frac{T^{dry}}{1 - \frac{R}{\Delta\hat{S}^f} ln\left(1 - X^{melt}_{water}\right)} \quad (2)$$

where T^{dry} is the temperature of dry melting of eclogite (taken from Yasuda et al., 1994), R is the universal gas constant, $\Delta\hat{S}^f$ is the molar entropy of fusion and X^{melt}_{water} is the molar fraction of total water (molecular H_2O + OH^-) in the melt at the solidus. As of today, no data are available in the literature regarding $\Delta\hat{S}^f$ of eclogite, but estimates of $\Delta\hat{S}^f$ of eclogite can be made. Kojitani & Akaogi (1995, 1997) reported values of ~0.31–0.36 $Jg^{-1}K^{-1}$ for the entropy of fusion (per unit weight, ΔS^f) of a basalt and 0.4 $Jg^{-1}K^{-1}$ for the ΔS^f of peridotite. Blundy et al. (1995) reported $\Delta\hat{S}^f$ of jadeite to be 64.8 $Jmol^{-1}K^{-1}$, which is notably lower than the 82.5 $Jmol^{-1}K^{-1}$ determined for diopside by Richet & Bottinga (1984). Since a jadeitic component is present in eclogitic clinopyroxenes, it is reasonable to expect a lower ΔS^f for eclogites compared to peridotites. Accordingly, the calculations performed in this study used a value of 0.35 $Jg^{-1}K^{-1}$, which is in the range given by Kojitani & Akaogi (1995) for a basalt. The model described here considers a melt molecule with 1 oxygen atom, and the molar mass was taken as 36.9 $gmol^{-1}$, following Hirschmann et al. (2009) for an 8-oxygen molecule (295 $gmol^{-1}$). The choice of the size of the melt molecule also influences the molar fraction of H_2O dissolved in the melt, as heavier melt molecules will result in a greater molar fraction of water compared to light melt molecules. To calculate the molar fraction of water in the melt, knowledge of the expected water content of the melt at the solidus is necessary, and this is obtained by combining the batch melting equation (for a melt fraction F = 0) with $D^{eclo/melt}_{H_2O}$. $D^{eclo/melt}_{H_2O}$ was calculated considering an eclogite consisting only of garnet and clinopyroxene. The abundance of garnet and clinopyroxene as a function of pressure at subsolidus conditions (i.e., 1000 °C) was modelled using Perple_X (Connolly, 2005, 2009) with the hp02ver database (Ghiorso et al., 2002; Holland & Powell, 1998) for the composition of AC74 (Aubaud et al., 2008). The calculated abundances were then fitted as a function of pressure with a third-degree polynomial (R^2 = 0.999) and result in a garnet abundance going from 37 wt% at 2 GPa to 52 wt% at 8 GPa. Since garnet did not crystallize in the experiments described in this work, the calculation used data from the experiments of Aubaud et al. (2008). Specifically, $D^{grt/melt}_{H_2O}$ was calculated using the $D^{grt/cpx}_{H_2O}$ (=0.097) measured by Aubaud et al. (2008). This should provide reliable results since, according to Keppler & Bolfan-Casanova (2006), the H_2O partition coefficient between any two phases α and β is described thermodynamically by:

$$D^{\alpha/\beta}_{H_2O} = \frac{A_\alpha}{A_\beta} f^{n_\alpha - n_\beta}_{H_2O} exp\left(-\frac{\left(\Delta H^{1bar}_\alpha - \Delta H^{1bar}_\beta\right) + \left(\Delta V^{solid}_\alpha - \Delta V^{solid}_\beta\right)P}{RT}\right) \quad (3)$$

where A_α and A_β are constants, n_α and n_β are exponents that depend on the dissolution mechanism of H in the mineral, ΔH^{1bar} are the reaction enthalpies at 1 bar, and ΔV^{solid} is the volume change of the solids. In fact, experimental studies showed that n = 0.5 for both clinopyroxene (Bromiley et al., 2004; Bromiley & Keppler, 2004) and garnet (Lu & Keppler, 1997), which implies that $f^{n_\alpha - n_\beta}_{H_2O} = f^{0.5-0.5}_{H_2O} = f^0_{H_2O}$ and, therefore, $D^{grt/cpx}_{H_2O}$ should be insensitive to both H_2O fugacity and CO_2 content. Consequently, $D^{grt/cpx}_{H_2O}$ is expected to remain constant around 0.097 (at a given temperature and pressure) regardless of the H_2O and CO_2 concentration in the system, assuming that the dissolution mechanism of H does not change as H_2O or CO_2 concentration is changed. $D^{eclo/melt}_{H_2O}$ was then calculated as a function of pressure by combining $D^{cpx/melt}_{H_2O}$ measured here with $D^{grt/cpx}_{H_2O}$ measured by Aubaud et al. (2008) and the garnet abundance modelled using Perple_X.

Conventionally, when calculating the melting point depression, water in the melt is assumed to be completely dissociated into OH^-, with no molecular H_2O present in the melt. This leads to a maximization of X^{melt}_{water}, since the number of OH^- moles is calculated as $n_{OH^-} = 2^*\left(n_{H_2O_{tot}} - n_{H_2O_{mol}}\right)$, and could potentially result in overestimating the effect of H_2O on the depression of the melting point of a rock (see Eq. (2)). The model developed in this study used the non-ideal thermodynamic speciation approach detailed by Silver & Stolper (1989), recalibrated for basalts up to high total water concentrations (see supplementary material) to determine the expected molecular H_2O and

OH^- concentrations at the total H_2O content of the melt at the solidus, calculated from the batch melting equation. Following this approach and Eq. (2), the hydrated solidus of an eclogite with 600 ppm wt H_2O (in agreement with measurements on natural samples, Nadeau et al., 1993) was calculated (Fig. 6) and results in a depression of the melting temperature caused by the presence of H_2O up to ~100 °C.

When C is added to the system, however, the situation changes dramatically, and both the melting temperature and reactions will differ from the purely hydrous scenario. Due to the extremely low solubility of C in NAMs (Keppler et al., 2003; Shcheka et al., 2006), at pressures >2 GPa carbonate minerals will be the hosts of C in eclogite (Dasgupta et al., 2004), provided that f_{O_2} is sufficiently high. If this is the case then the solidus of the rock will be controlled by that of the carbonate minerals and the first melt forming at the solidus will be carbonatitic (Dasgupta, 2018; Dasgupta et al., 2004, 2013, 2022; Hammouda, 2003; Hammouda & Keshav, 2015). H_2O starts playing a role in the melting of the rock at the onset of silicate melting, which starts when the CO_2 concentration in the melt (CO_2^{melt}) is ~25 wt% (Dasgupta et al., 2013). Here, the parametrization of Dasgupta et al. (2013) is used to calculate the temperature at which a melt with CO_2^{melt} = 25 wt% is expected to form (T^{carb}; Fig. 6) from an eclogite with a bulk H_2O content of 600 ppm wt, and a CO_2 content of 67 and 300 ppm wt (corresponding to $XCO_2 = 0.1$ and 0.33, respectively). Then, $D_{H_2O}^{eclo/melt}$ in the presence of CO_2 is used to calculate the concentration of H_2O in the carbonated-silicate melt and, using the cryoscopic equation (Eq. (2)) substituting T^{dry} with T^{carb}, the melting temperature of a hydrous-carbonated eclogite in the mantle is calculated (Fig. 6).

The melting temperature calculated using Eq. (2) ranges from 1003 °C at 2 GPa to 1171 °C at 8 GPa for an eclogite with 600 ppm wt H_2O and 67 ppm wt CO_2 ($XCO_2 = 0.1$) and from 975 °C at 2 GPa to 1132 °C at 8 GPa for an eclogite with 600 ppm wt H_2O and 300 ppm wt CO_2 ($XCO_2 = 0.33$). The temperature of carbonated melting as well as those of hydrous-carbonated melting are always lower than the temperature of an adiabatic geotherm (Katsura, 2022) implying that, in the presence of carbonates, partial melting of an eclogite is possible even in the deep upper mantle. Moreover, the hydrous carbonated melting temperature of the system with $XCO_2 = 0.33$ crosses the pressure–temperature path of the hottest subduction (i.e., Cascadia; Syracuse et al., 2010) at ~5.8 GPa (Fig. 6a), suggesting that melting of the crust of a hot subducting slab can occur at P > 5.8 GPa. Similarly, if eclogites in the cratonic continental lithosphere are considered (Fig. 6b), hydrous carbonated partial melting would occur along the 35, 40 and 45 mW/m^2 conductive geotherms (Hasterok & Chapman, 2011) at pressures around 6.3, 4.4 and 3.3 GPa, respectively (for a system with $XCO_2 = 0.33$).

Such low melting temperatures would have important implications for the geochemistry of the mantle, as melts generated in these scenarios will be enriched in volatiles as well as SiO_2 (Pertermann & Hirschmann, 2003) and could easily migrate in the mantle to metasomatize surrounding rocks. However, some important considerations must be taken into account regarding the models presented here and their implications. First, the parametrization used here for the temperature of carbonate melting as a function of CO_2^{melt} was proposed based on experiments performed on the melting of carbonated peridotite (Dasgupta et al., 2013). This means that, although the general principles should hold for eclogites as well as peridotites, the slope and location of the carbonated melting isopleth(s) may be different. Moreover, the entire melting model is centered around the assumption that carbonates are the stable C-bearing phases at all the conditions considered. This however might not be the case, as f_{O_2} is well-known to decrease with depth in the mantle (Frost & McCammon, 2008), and once f_{O_2} becomes lower than the DCDG/D (dolomite-coesite-diopside-graphite/diamond; Luth, 1993) buffer, carbonates are no longer the stable C-bearing phase in an eclogite, and are substituted by graphite or diamond, depending on the P-T conditions. In this scenario C is immobilized and does not participate in melting reactions, and therefore the solidus becomes that of a hydrous eclogite. This is probably the case for eclogites located in the cratonic lithosphere, since analyses on eclogitic xenoliths from different cratonic areas show that, regardless of the depth, eclogites always exhibit f_{O_2} conditions lower than the DCDG/D buffer (Aulbach & Smart, 2023). The situation is more complex for subducting slabs where f_{O_2} is not as accurately known as for the continental lithosphere. If the

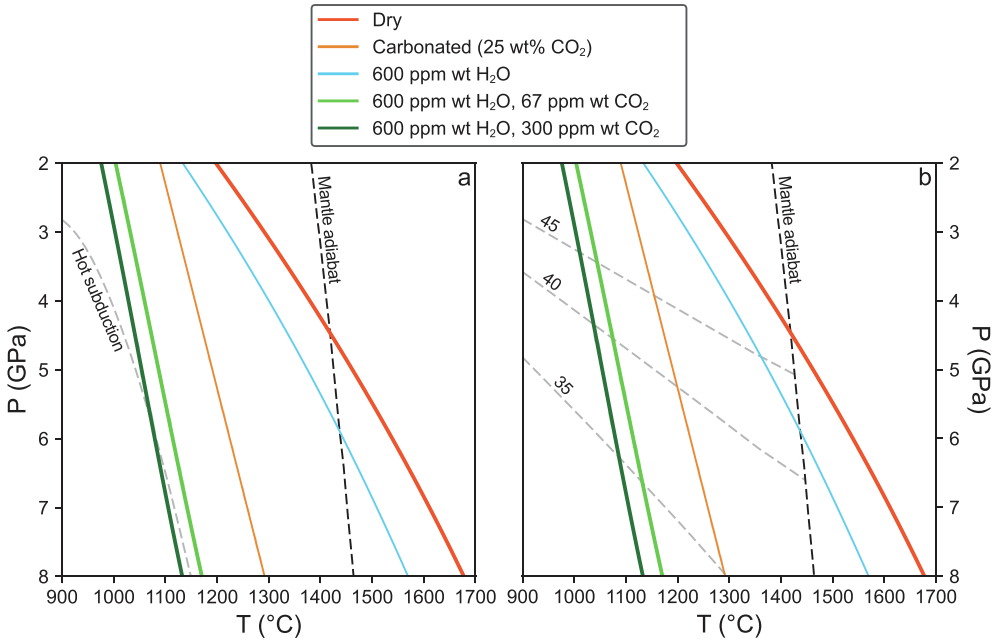

Fig. 6. Solidus of eclogite modelled at different H_2O and CO_2 concentration using the parametrization by (Dasgupta et al., 2013) and the cryoscopic equation (see text). The dry solidus is from experiments of Yasuda et al. (1994). The "Carbonated (25 wt% CO_2)" line represents the temperature required to generate a silicate-carbonated melt with CO_2^{melt} = 25 wt%. The black dashed line represents a mantle adiabat after Katsura (2022). (a) The grey dashed line represents the temperature of the hottest subduction (i.e., Cascadia, from Syracuse et al., 2010). (b) The grey dashed lines represent the conductive geotherms for a surface heat flow of 35, 40 and 45 mW/m^2 (from Hasterok & Chapman, 2011).

amount of Fe^{3+} ($Fe^{3+}/\sum Fe$) in the subducting oceanic crust is assumed to be the same as observed in MORB glasses ($Fe^{3+}/\sum Fe = 0.12 \pm 0.2$; Bézos & Humler, 2005) then carbonates will be stable in the assemblage to pressures greater than ~6.5 GPa (Stagno et al., 2015) and melting will occur in hot subducting slabs. However, if dehydration reactions occur in the slab during subduction, oxidized species could be removed from the oceanic crust and transferred to the overlying mantle, causing a decrease in the oxidizing potential of the subducting slab (Frost & McCammon, 2008). If during subduction $Fe^{3+}/\sum Fe$ of the slab decreases to values ~0.05, graphite/diamond will be stable well above the ~5.8 GPa threshold (Stagno et al., 2015) that marks the onset of hydrous-carbonated melting in the slab and melting will therefore, in principle, not occur. However, even in cases where graphite/diamond should be stable, carbonates could still be present in the assemblage as their reduction into C would require oxidation of large amounts of FeO, which will occur in large depth intervals (Stagno et al., 2015), and melting could therefore still take place in a subducting crust with low $Fe^{3+}/\sum Fe$.

4.2. H_2O concentration in a mantle source for HIMU domains

It is generally accepted that the distribution of volatiles in the mantle is heterogeneous, with deeper regions of the mantle sampled by plumes generating OIBs that appear to be H_2O rich (750 ppm wt H_2O) as opposed to the shallower, convective mantle producing MORBs having a lower H_2O content (290 ppm wt H_2O, Hirschmann, 2018). An H_2O enrichment of the deep mantle may be related to the recycling of hydrated lithospheric material at subduction zones (e.g., Pamato et al., 2015). Isotopic constraints have further determined the existence of different reservoir endmembers, such as HIMU (High-μ) and EM (Enriched Mantle), sampled by OIBs. The EM endmember is characterized by high $^{87}Sr/^{86}Sr$ and low $^{143}Nd/^{144}Nd$ and $^{176}Hf/^{177}Hf$ (Stracke, 2012) and is thought to be associated with recycled crustal material (Stracke, 2012; Willbold & Stracke, 2010). On the other hand, the HIMU endmember is characterized by high values of μ ($\mu = {}^{238}U/^{204}Pb$; Stracke et al., 2005). The HIMU reservoir is often suggested to be derived from recycled oceanic crust, either pure or mixed to different degrees with the depleted mantle (Hauri & Hart, 1993; Hofmann & White, 1982; Stracke, 2012; Stracke et al., 2005), although other possible origins have been proposed for this reservoir, such as metasomatic alteration of the mantle (Hanyu et al., 2012; Hanyu & Kaneoka, 1998) or evolved lower mantle melting residues (Collerson et al., 2010). The HIMU reservoir is of particular interest since if it is assumed to be composed of (almost) pure recycled oceanic crust it would consist mainly of eclogite. Cabral et al. (2014) previously constrained the H_2O content of the HIMU mantle region by investigating homogenized alkali-basalt melt inclusions from Mangaia, Cook Islands, one of the few locations in the world representative of an extreme HIMU source mantle (Stracke et al., 2005; Woodhead, 1996). By determining the H_2O/Ce ratio of the melt inclusions (~200), Cabral et al. (2014) proposed a HIMU mantle source H_2O concentration of 440 ppm wt for a degree of melting F = 0.03, highlighting the presence of H_2O-rich regions in the deep mantle. This H_2O content was calculated assuming a relatively high (with respect to ambient mantle) bulk rock Ce content of 2.2 ppm wt derived by mixing ambient mantle with 20 % altered oceanic crust in the source. Further constraints on the H_2O contents of HIMU sources can be made by combining the H_2O content of the melt inclusions measured by Cabral et al. (2014) with the partition coefficients calculated in this work. This allows one to test whether partial melting of an eclogite can produce the volatile contents of HIMU-like melt inclusions of Cabral et al. (2014) with a simple mass balance model. This is particularly important in the case of HIMU sources, considering the high CO_2 concentrations measured in the inclusions (up to 2346 ppm wt) by Cabral et al. (2014), which are most likely minimum values given the evidence of extensive CO_2 degassing (Cabral et al., 2014).

An eclogite made of 55 % garnet and 45 % clinopyroxene (Aulbach & Jacob, 2016) was considered to represent altered oceanic crust, allowing calculation of $D_{H_2O}^{eclo/melt}$ using the same approach described in the section above. The fractional melting equation:

$$\frac{C_m}{C_b} = \frac{1-(1-F)^{1/D}}{F} \quad (4)$$

where C_m is the concentration of H_2O in the melt, C_b is the bulk rock H_2O concentration, F is the melt fraction and D is the rock-melt H_2O partition coefficient, was then used to calculate the H_2O in the melt source region necessary to produce a melt with 1.37 wt% H_2O as Cabral et al. (2014) observed. Calculations were performed considering a range of melt fractions (F = 0–0.1) and at $XCO_2 = 0$, 0.1 and 0.3; results are shown in Fig. 7. The bulk H_2O concentrations calculated at different XCO_2 (and hence different calculated $D_{H_2O}^{eclo/melt}$) converge at melt fractions F = ~0.08–0.1, making the effect of CO_2 on $D_{H_2O}^{eclo/melt}$ irrelevant. To obtain some relevant estimates of the H_2O concentration in the source of the magma it is necessary to constrain the melt fraction to a relatively small interval. A boundary for F was determined by considering the Ce concentration of the melt inclusions, measured by Cabral et al. (2014) to be 68.5 ppm wt. Eclogite xenoliths have been shown to have a median Ce concentration of 2.8 ppm wt (Aulbach & Jacob, 2016), and values up to 6 ppm wt Ce are reported in the literature (Nadeau et al., 1993). Using Ce partition coefficients for eclogitic garnet and clinopyroxene from Klemme et al. (2002) and the fractional melting equation constrains F between 0.02 and 0.08 to produce melts with 68.5 ppm wt Ce starting from an eclogite with a bulk Ce content between 2.8 and 6 ppm wt. Moreover, petrologic models for the production of OIBs show that volatile-enriched sources should be restricted to F < 0.05 (Herzberg & Gazel, 2009), making melt fractions greater than these an uncommon occurrence.

For this model both the geochemical and petrological constraints were combined and the melt fraction considered was thus restricted to a range between ~0.02 (the lower boundary provided by Ce partitioning calculations) and ~0.05 (the higher boundary provided by petrologic models). The resulting bulk H_2O concentration in the melt source region

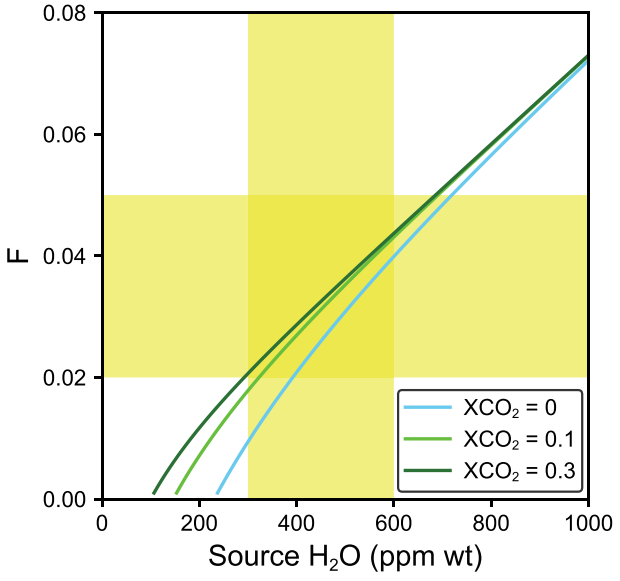

Fig. 7. Bulk H_2O concentration required for a 45% clinopyroxene and 55% garnet eclogite to produce magmas with the H_2O concentration measured by Cabral et al. (2014), using the $D_{H_2O}^{eclo/melt}$ calculated in this work for different XCO_2 and as a function of the melt fraction (F). The two yellow shaded areas represent the most likely F involved in the production of the magma in question and the range of bulk H_2O concentrations reported in the literature for nominally anhydrous eclogites (see text).

is estimated to vary between ~300 and ~720 ppm wt, in agreement with the range of H_2O concentrations measured in eclogite xenoliths in the literature (300–600 ppm wt; Katayama et al., 2006; Nadeau et al., 1993).

This simple melting model shows how low degree partial melting of hydrous-carbonated eclogites can produce magmas with H_2O contents matching those measured in magmas from HIMU mantle domains. Although melting of pure eclogite could produce melts with H_2O contents such as those measured by Cabral et al. (2014), isotopic evidence supports the presence of at least a fraction of peridotite component in HIMU reservoirs (Hauri & Hart, 1993). In the case of partial melting of both eclogite and peridotite, a magma with 1.37 wt% H_2O could still be produced with realistic H_2O contents in the source (depending on F). Therefore, the presence of both eclogite and peridotite in HIMU reservoirs cannot be ruled out.

5. Conclusions

Experiments were conducted to quantify the effect of CO_2 on $D_{H_2O}^{cpx/melt}$ at 2 GPa and 1200 °C. The experiments produced large clinopyroxene crystals in equilibrium with a quenched hydrous or hydrous-carbonated basaltic-andesitic melt that allowed precise H_2O and CO_2 contents to be determined. The $D_{H_2O}^{cpx/melt}$ is observed to decrease from 0.029 to 0.017 when XCO_2 increases to 0.34, with a rapid decrease observed from $XCO_2 = 0$ to $XCO_2 = 0.2$, and values remaining constant at $XCO_2 > 0.2$. This behavior was fitted with a negative power law in the form of $D_{H_2O}^{cpx/melt} = 0.0123*XCO_2^{-0.237}$. This equation shows how the presence of CO_2 can have dramatic effects on the H_2O storage capacity of Earth's mantle. Using the equation obtained in this work together with models for carbonated melting, the presence of CO_2 in an eclogite was calculated to lower the melting temperature by 100s of °C. This implies that, along a normal mantle adiabatic geotherm, melting of eclogitic lithologies could occur in the deep upper mantle and that a hot subducting slab will start melting at P > 5.8 GPa, provided carbonates are still present in the assemblage. The $D_{H_2O}^{cpx/melt}$ values further allow calculations of the bulk mantle source concentration for HIMU magmas as a function of the CO_2 concentration and melt fraction involved in the production of the magma. A simple mass balance model indicates that a CO_2-bearing eclogitic mantle source with H_2O concentrations ranging from 300 to 720 ppm wt can form a magma with the same H_2O concentration observed in HIMU magmas.

CRediT authorship contribution statement

Andrea Curtolo: Writing – original draft, Visualization, Software, Methodology, Investigation, Formal analysis, Data curation. **Pierre Condamine:** Writing – review & editing, Investigation, Formal analysis. **Federica Schiavi:** Writing – review & editing, Investigation, Formal analysis, Data curation. **Nathalie Bolfan-Casanova:** Writing – review & editing, Validation. **Davide Novella:** Writing – review & editing, Supervision, Conceptualization.

Declaration of competing interest

The authors declare that they have no known competing financial interests or personal relationships that could have appeared to influence the work reported in this paper.

Acknowledgements

The authors thank Rajdeep Dasgupta, David Neave and a third, anonymous reviewer for providing valuable comments that improved the quality of this manuscript and Olivier Namur for editorial handling. The authors also thank the LG-SIMS-Nancy team for assistance with the SIMS analyses and discussions and Jean-Luc Devidal for the assistance with the microprobe analyses.

This is contribution no. 691 of the ClerVolc program of the International Research Center for Disaster Sciences and Sustainable Development of the University of Clermont Auvergne, supported by the Agence Nationale de la Recherche. The Graduate Track of Involc is also thanked for funding visiting of A.C. at LMV.

Appendix A. Supplementary material

Supplementary Material I for this work consists of Tables S1–S4 and Figs. S1–S9, all cited in the main text and contained in a single pdf file. Supplementary Material II consists of a pdf file with details about the statistical model for assessment of the accuracy of FTIR measurements on clinopyroxenes (Appendix I) and the new calibration of the water speciation model in basalts (Appendix II), along with Figs. S10 and S11, cited in the text of Appendix I. Supplementary material to this article can be found online at https://doi.org/10.1016/j.gca.2025.03.013.

Data availability

Data are available through the University of Padova online repository at https://researchdata.cab.unipd.it/id/eprint/1502.

References

Adam, J., Turner, M., Hauri, E.H., Turner, S., 2016. Crystal/melt partitioning of water and other volatiles during the near-solidus melting of mantle peridotite: comparisons with non-volatile incompatible elements and implications for the generation of intraplate magmatism. Am. Mineral. 101 (4), 876–888.

Aubaud, C., Hauri, E.H., Hirschmann, M.M., 2004. Hydrogen partition coefficients between nominally anhydrous minerals and basaltic melts. Geophys. Res. Lett. 31 (20), L20611.

Aubaud, C., Hirschmann, M.M., Withers, A.C., Hervig, R.L., 2008. Hydrogen partitioning between melt, clinopyroxene, and garnet at 3 GPa in a hydrous MORB with 6 wt.% H_2O. Contrib. Miner. Petrol. 156 (5), 607–625.

Aulbach, S., Jacob, D.E., 2016. Major- and trace-elements in cratonic mantle eclogites and pyroxenites reveal heterogeneous sources and metamorphic processing of low-pressure protoliths. Lithos 262, 586–605.

Aulbach, S., Smart, K.A., 2023. Petrogenesis and Geodynamic Significance of Xenolithic Eclogites. Annu. Rev. Earth Planet. Sci. 51, 521–549.

Baptiste, V., Demouchy, S., Keshav, S., Parat, F., Bolfan-Casanova, N., Condamine, P., Cordier, P., 2015. Decrease of hydrogen incorporation in forsterite from CO_2-H_2O-rich kimberlitic liquid. Am. Mineral. 100 (8–9), 1912–1920.

Bell, D.R., Ihinger, P.D., Rossman, G.R., 1995. Quantitative analysis of trace OH in garnet and pyroxenes. Am. Mineral. 80 (5–6), 465–474.

Beran, A., Libowitzky, E., 2006. Water in natural mantle minerals II: olivine, garnet and accessory minerals. In: Keppler, H., Smyth, J.R. (Eds.), Water in Nominally Anhydrous Minerals. De Gruyter, pp. 169–191.

Bézos, A., Humler, E., 2005. The $Fe^{3+}/\Sigma Fe$ ratios of MORB glasses and their implications for mantle melting. Geochim. Cosmochim. Acta 69 (3), 711–725.

Blundy, J.D., Falloon, T.J., Wood, B.J., Dalton, J.A., 1995. Sodium partitioning between clinopyroxene and silicate melts. J. Geophys. Res. 100 (B8), 501–515.

Bolfan-Casanova, N., 2005. Water in the Earth's mantle. Mineral. Mag. 69 (3), 229–257.

Bromiley, G.D., Keppler, H., 2004. An experimental investigation of hydroxyl solubility in jadeite and Na-rich clinopyroxenes. Contrib. Miner. Petrol. 147 (2), 189–200.

Bromiley, G.D., Keppler, H., McCammon, C., Bromiley, F.A., Jacobsen, S.D., 2004. Hydrogen solubility and speciation in natural, gem-quality chromian diopside. Am. Mineral. 89 (7), 941–949.

Buso, R., Laporte, D., Schiavi, F., Cluzel, N., Fonquernie, C., 2022. High-pressure homogenization of olivine-hosted CO_2-rich melt inclusions in a piston cylinder: insight into the volatile content of primary mantle melts. Eur. J. Mineral. 34 (3), 325–349.

Cabral, R.A., Jackson, M.G., Koga, K.T., Rose-Koga, E.F., Hauri, E.H., Whitehouse, M.J., Price, A.A., Day, J.M.D., Shimizu, N., Kelley, K.A., 2014. Volatile cycling of H_2O, CO_2, F, and Cl in the HIMU mantle: a new window provided by melt inclusions from oceanic hot spot lavas at Mangaia, Cook Islands. Geochem. Geophys. Geosyst. 15 (11), 4445–4467.

Cartigny, P., Pineau, F., Aubaud, C., Javoy, M., 2008. Towards a consistent mantle carbon flux estimate: insights from volatile systematics (H_2O/Ce, δD, CO_2/Nb) in the North Atlantic mantle (14° N and 34° N). Earth Planet. Sci. Lett. 265 (3–4), 672–685.

Collerson, K.D., Williams, Q., Ewart, A.E., Murphy, D.T., 2010. Origin of HIMU and EM-1 domains sampled by ocean island basalts, kimberlites and carbonatites: the role of CO_2-fluxed lower mantle melting in thermochemical upwellings. Phys. Earth Planet. In. 181 (3–4), 112–131.

Connolly, J.A.D., 2005. Computation of phase equilibria by linear programming: a tool for geodynamic modeling and its application to subduction zone decarbonation. Earth Planet. Sci. Lett. 236 (1–2), 524–541.

Connolly, J.A.D., 2009. The geodynamic equation of state: what and how. Geochem. Geophys. Geosyst. 10 (10), Q10014.
Dasgupta, R., 2013. Ingassing, storage, and outgassing of terrestrial carbon through geologic time. In: Hazen, R.M., Jones, A.P., Baross, J.A. (Eds.), Carbon in earth. De Gruyter, pp. 183–229.
Dasgupta, R., 2018. Volatile-bearing partial melts beneath oceans and continents–Where, how much, and of what compositions? Am. J. Sci. 318 (1), 141–165.
Dasgupta, R., Hirschmann, M.M., Withers, A.C., 2004. Deep global cycling of carbon constrained by the solidus of anhydrous, carbonated eclogite under upper mantle conditions. Earth Planet. Sci. Lett. 227 (1–2), 73–85.
Dasgupta, R., Hirschmann, M.M., Smith, N.D., 2007. Water follows carbon: CO_2 incites deep silicate melting and dehydration beneath mid-ocean ridges. Geology 35 (2), 135–138.
Dasgupta, R., Mallik, A., Tsuno, K., Withers, A.C., Hirth, G., Hirschmann, M.M., 2013. Carbon-dioxide-rich silicate melt in the Earth's upper mantle. Nature 493 (7431), 211–215.
Dasgupta, R., Chowdhury, P., Eguchi, J., Sun, C., Saha, S., 2022. Volatile-bearing partial melts in the lithospheric and sub-lithospheric mantle on earth and other rocky planets. In: Neuville, D.R., Henderson, G.S., Dingwell, D.B. (Eds.), Geological Melts. De Gruyter, pp. 575–606.
DeVitre, C.L., Gazel, E., Ramalho, R.S., Venugopal, S., Steele-MacInnis, M., Hua, J., Allison, C.M., Moore, L.R., Carracedo, J.C., Monteleone, B., 2023. Oceanic intraplate explosive eruptions fed directly from the mantle. Proc. Natl. Acad. Sci. 120 (33), e2302093120.
Dixon, J.E., Stolper, E.M., Holloway, J.R., 1995. An experimental study of water and carbon dioxide solubilities in mid-ocean ridge basaltic liquids. Part I: calibration and solubility models. J. Petrol. 36 (6), 1607–1631.
Dixon, J.E., Clague, D.A., Wallace, P., Poreda, R., 1997. Volatiles in alkalic basalts from the North arch volcanic field, hawaii: extensive degassing of deep submarine-erupted alkalic series lavas. J. Petrol. 38 (7), 911–939.
Dvir, O., Kessel, R., 2017. The effect of CO_2 on the water-saturated solidus of K-poor peridotite between 4 and 6 GPa. Geochim. Cosmochim. Acta 206, 184–200.
Elazar, O., Frost, D., Navon, O., Kessel, R., 2019. Melting of H_2O and CO_2-bearing eclogite at 4–6 GPa and 900–1200 °C: implications for the generation of diamond-forming fluids. Geochim. Cosmochim. Acta 255, 69–87.
Fine, G., Stolper, E., 1985. Dissolved carbon dioxide in basaltic glasses: concentrations and speciation. Earth Planet. Sci. Lett. 76, 263–278.
Fischer, T.P., Arellano, S., Carn, S., Aiuppa, A., Galle, B., Allard, P., Lopez, T., Shinohara, H., Kelly, P., Werner, C., Cardellini, C., Chiodini, G., 2019. The emissions of CO_2 and other volatiles from the world's subaerial volcanoes. Sci. Rep. 9 (1), 18716.
Foley, S.F., Yaxley, G.M., Rosenthal, A., Buhre, S., Kiseeva, E.S., Rapp, R.P., Jacob, D.E., 2009. The composition of near-solidus melts of peridotite in the presence of CO_2 and H_2O between 40 and 60 kbar. Lithos 112, 274–283.
Frost, D.J., McCammon, C.A., 2008. The Redox State of earth's mantle. Annu. Rev. Earth Planet. Sci. 36, 389–420.
Gaillard, F., Bouhifd, M.A., Füri, E., Malavergne, V., Marrocchi, Y., Noack, L., Ortenzi, G., Roskosz, M., Vulpius, S., 2021. The diverse planetary ingassing/outgassing paths produced over billions of years of magmatic activity. Space Sci. Rev. 217 (1), 22.
Ghiorso, M.S., Hirschmann, M.M., Reiners, P.W., Kress, V.C., 2002. The pMELTS: a revision of MELTS for improved calculation of phase relations and major element partitioning related to partial melting of the mantle to 3 GPa. Geochem. Geophys. Geosyst. 3 (5), 1–35.
Green, D.H., 1973. Experimental melting studies on a model upper mantle composition at high pressure under water-saturated and water-undersaturated conditions. Earth Planet. Sci. Lett. 19 (1), 37–53.
Guo, X., Bai, J., Wang, C., Wu, X., Zhou, X., 2020. CO_2 induced a small water solubility in orthopyroxene and its implications for water storage in the upper mantle. J. Geophys. Res. Solid Earth 125 (2), e2021JB018745.
Hammouda, T., 2003. High-pressure melting of carbonated eclogite and experimental constraints on carbon recycling and storage in the mantle. Earth Planet. Sci. Lett. 214 (1–2), 357–368.
Hammouda, T., Keshav, S., 2015. Melting in the mantle in the presence of carbon: review of experiments and discussion on the origin of carbonatites. Chem. Geol. 418, 171–188.
Hanyu, T., Kaneoka, I., 1998. Open system behavior of helium in case of the HIMU source area. Geophys. Res. Lett. 25 (5), 687–690.
Hanyu, T., Tatsumi, Y., Senda, R., Miyazaki, T., Chang, Q., Hirahara, Y., Takahashi, T., Kawabata, H., Suzuki, K., Kimura, J.I., Nakai, S., 2012. Geochemical characteristics and origin of the HIMU reservoir: a possible mantle plume source in the lower mantle. Geochem. Geophys. Geosyst. 12 (2), Q0AC09.
Hasterok, D., Chapman, D.S., 2011. Heat production and geotherms for the continental lithosphere. Earth Planet. Sci. Lett. 307 (1–2), 59–70.
Hauri, E.H., Hart, S.R., 1993. Re-Os isotope systematics of HIMU and EMII oceanic island basalts from the south Pacific Ocean. Earth Planet. Sci. Lett. 114, 353–371.
Hauri, E.H., Gaetani, G.A., Green, T.H., 2006. Partitioning of water during melting of the Earth's upper mantle at H_2O-undersaturated conditions. Earth Planet. Sci. Lett. 248 (3–4), 715–734.
Herzberg, C., Gazel, E., 2009. Petrological evidence for secular cooling in mantle plumes. Nature 458 (7238), 619–622.
Hirschmann, M.M., 2018. Comparative deep Earth volatile cycles: the case for C recycling from exosphere/mantle fractionation of major (H_2O, C, N) volatiles and from H_2O/Ce, CO_2/Ba, and CO_2/Nb exosphere ratios. Earth Planet. Sci. Lett. 502, 262–273.
Hirschmann, M.M., Tenner, T., Aubaud, C., Withers, A.C., 2009. Dehydration melting of nominally anhydrous mantle: the primacy of partitioning. Phys. Earth Planet. In. 176 (1–2), 54–68.
Hofmann, A.W., White, W.M., 1982. Mantle plumes from ancient oceanic crust. Earth Planet. Sci. Lett. 57 (2), 421–436.
Holland, T.J.B., Powell, R., 1998. An internally consistent thermodynamic data set for phases of petrological interest. J. Metam. Geol. 16 (3), 309–343.
Ingrin, J., Blanchard, M., 2006. Diffusion of hydrogen in minerals. In: Keppler, H., Smyth, J.R. (Eds.), Water in Nominally Anhydrous Minerals. De Gruyter, pp. 291–320.
Jacobsen, S.D., 2006. Effect of water on the equation of state of nominally anhydrous minerals. In: Keppler, H., Smyth, J.R. (Eds.), Water in Nominally Anhydrous Minerals. De Gruyter, pp. 321–342.
Jambon, A., 1994. Earth degassing and large-scale geochemical cycling of volatile elements. In: Carrol, M.R., Holloway, J.H. (Eds.), Volatiles in Magmas. De Gruyter, pp. 479–518.
Jarrard, R.D., 2003. Subduction fluxes of water, carbon dioxide, chlorine, and potassium. Geochem. Geophys. Geosyst. 4 (5), 8905.
Katayama, I., Nakashima, S., Yurimoto, H., 2006. Water content in natural eclogite and implication for water transport into the deep upper mantle. Lithos 86 (3–4), 245–259.
Katsura, T., 2022. A revised adiabatic temperature profile for the mantle. J. Geophys. Res. Solid Earth 127, e2021JB023562.
Keppler, H., Bolfan-Casanova, N., 2006. Thermodynamics of water solubility and partitioning. In: Keppler, H., Smyth, J.R. (Eds.), Water in Nominally Anhydrous Minerals. De Gruyter, pp. 193–230.
Keppler, H., Wiedenbeck, M., Shcheka, S.S., 2003. Carbon solubility in olivine and the mode of carbon storage in the Earth's mantle. Nature 424 (6947), 414–416.
Kingsley, R.H., Schilling, J.-G., 1995. Carbon in Mid-Atlantic Ridge basalt glasses from 28°N to 63°N: evidence for a carbon-enriched Azores mantle plume. Earth Planet. Sci. Lett. 129 (1–4), 31–53.
Klemme, S., Blundy, J.D., Wood, B.J., 2002. Experimental constraints on major and trace element partitioning during partial melting of eclogite. Geochim. Cosmochim. Acta 66 (17), 3109–3123.
Koch-Müller, M., Abs-Wurmbach, I., Rhede, D., Kahlenberg, V., Matsyuk, S., 2007. Dehydration experiments on natural omphacites: qualitative and quantitative characterization by various spectroscopic methods. Phys. Chem. Miner. 34 (9), 663–678.
Koga, K., Hauri, E., Hirschmann, M., Bell, D., 2003. Hydrogen concentration analyses using SIMS and FTIR: comparison and calibration for nominally anhydrous minerals. Geochem. Geophys. Geosyst. 4 (2), 1019.
Kohlstedt, D.L., 2006. The role of water in high-temperature rock deformation. In: Keppler, H., Smyth, J.R. (Eds.), Water in Nominally Anhydrous Minerals. De Gruyter, pp. 377–396.
Kohlstedt, D.L., Keppler, H., Rubie, D.C., 1996. Solubility of water in the α, β and γ phases of $(Mg,Fe)_2SiO_4$. Contrib. Miner. Petrol. 123, 345–357.
Kojitani, H., Akaogi, M., 1995. Measurement of heat of fusion of model basalt in the system Diopside-forsterite-anorthite. Geophys. Res. Lett. 22 (17), 2329–2332.
Kojitani, H., Akaogi, M., 1997. Melting enthalpies of mantle peridotite: calorimetric determinations in the system CaO-MgO-Al_2O_3-SiO_2 and application to magma generation. Earth Planet. Sci. Lett. 153 (3–4), 209–222.
Lara, M., Dasgupta, R., 2023. Effects of H_2O-CO_2 fluids, temperature, and peridotite fertility on partial melting in mantle wedges and generation of primary arc basalts. J. Petrol. 64 (7), 1–20.
Le Voyer, M., Kelley, K.A., Cottrell, E., Hauri, E.H., 2017. Heterogeneity in mantle carbon content from CO_2-undersaturated basalts. Nat. Commun. 8, 14062.
Le Voyer, M., Hauri, E.H., Cottrell, E., Kelley, K.A., Salters, V.J.M., Langmuir, C.H., Hilton, D.R., Barry, P.H., Füri, E., 2019. Carbon fluxes and primary magma CO_2 contents along the global mid-ocean ridge system. Geochem. Geophys. Geosyst. 20 (3), 1387–1424.
Libowitzky, E., Rossman, G.R., 1996. Principles of quantitative absorbance measurements in anisotropic crystals. Phys. Chem. Miner. 23, 319–327.
Libowitzky, E., Rossman, G.R., 1997. An IR absorption calibration for water in minerals. Am. Mineral. 82 (11–12), 1111–1115.
Ligi, M., Bonatti, E., Cipriani, A., Ottolini, L., 2005. Water-rich basalts at mid-ocean-ridge cold spots. Nature 434 (7029), 66–69.
Lu, R., Keppler, H., 1997. Water solubility in pyrope to 100 kbar. Contrib. Miner. Petrol. 129, 35–42.
Luth, R.W., 1993. Diamonds, Eclogites, and the oxidation state of the earth's mantle. Science 261 (5117), 66–68.
McMillan, P.F., 1994. Water solubility and speciation models. In: Carroll, M.R., Holloway, J.R. (Eds.), Volatiles in Magmas. De Gruyter, pp. 131–156.
Mierdel, K., Keppler, H., Smyth, J.R., Langenhorst, F., 2007. Water solubility in aluminous orthopyroxene and the origin of earth's asthenosphere. Science 315 (5810), 364–368.
Mosenfelder, J.L., Rossman, G.R., 2013. Analysis of hydrogen and fluorine in pyroxenes: II. Clinopyroxene. Am. Miner. 98 (5–6), 1042–1054.
Myhill, R., Frost, D.J., Novella, D., 2017. Hydrous melting and partitioning in and above the mantle transition zone: insights from water-rich MgO–SiO_2–H_2O experiments. Geochim. Cosmochim. Acta 200, 408–421.
Nadeau, S., Philippot, P., Pineau, F., 1993. Fluid inclusion and mineral isotopic compositions (H-C-O) in eclogitic rocks as tracers of local fluid migration during high-pressure metamorphism. Earth Planet. Sci. Lett. 114, 431–448.
Ni, H., Keppler, H., 2013. Carbon in silicate melts. In: Hazen, R.M., Jones, A.P., Baross, J. A. (Eds.), Carbon in Earth. De Gruyter, pp. 251–287.

Novella, D., Frost, D.J., 2014. The composition of hydrous partial melts of garnet peridotite at 6GPa: implications for the origin of group II Kimberlites. J. Petrol. 55 (11), 2097–2124.
Novella, D., Frost, D.J., Hauri, E.H., Bureau, H., Raepsaet, C., Roberge, M., 2014. The distribution of H_2O between silicate melt and nominally anhydrous peridotite and the onset of hydrous melting in the deep upper mantle. Earth Planet. Sci. Lett. 400, 1–13.
Novella, D., Dolejš, D., Myhill, R., Pamato, M.G., Manthilake, G., Frost, D.J., 2017. Melting phase relations in the systems Mg_2SiO_4–H_2O and $MgSiO_3$–H_2O and the formation of hydrous melts in the upper mantle. Geochim. Cosmochim. Acta 204, 68–82.
O'Leary, J.A., Gaetani, G.A., Hauri, E.H., 2010. The effect of tetrahedral Al^{3+} on the partitioning of water between clinopyroxene and silicate melt. Earth Planet. Sci. Lett. 297 (1–2), 111–120.
Ohlhorst, S., Behrens, H., Holtz, F., 2001. Compositional dependence of molar absorptivities of near-infrared OH^- and H_2O bands in rhyolitic to basaltic glasses. Chem. Geol. 174 (1–3), 5–20.
Pamato, M.G., Myhill, R., Boffa Ballaran, T., Frost, D.J., Heidelbach, F., Miyajima, N., 2015. Lower-mantle water reservoir implied by the extreme stability of a hydrous aluminosilicate. Nat. Geosci. 8 (1), 75–79.
Pertermann, M., Hirschmann, M.M., 2003. Anhydrous partial melting experiments on MORB-like eclogite: phase relations, phase compositions and mineral-melt partitioning of major elements at 2-3 GPa. J. Petrol. 44 (12), 2173–2201.
Peslier, A.H., Luhr, J.F., Post, J., 2002. Low water contents in pyroxenes from spinel-peridotites of the oxidized, sub-arc mantle wedge. Earth Planet. Sci. Lett. 201 (1), 69–86.
Peslier, A.H., Schönbächler, M., Busemann, H., Karato, S.-I., 2017. Water in the Earth's Interior: distribution and Origin. Space Sci. Rev. 212 (1–2), 743–810.
Pintér, Z., Foley, S.F., Yaxley, G.M., Rosenthal, A., Rapp, R.P., Lanati, A.W., Rushmer, T., 2021. Experimental investigation of the composition of incipient melts in upper mantle peridotites in the presence of CO_2 and H_2O. Lithos 396–397, 106224.
Richet, P., Bottinga, Y., 1984. Anorthite, andesine, wollastonite, diopside, cordierite and pyrope: thermodynamics of melting, glass transitions, and properties of the amorphous phases. Earth Planet. Sci. Lett. 67, 415–432.
Schiavi, F., Bolfan-Casanova, N., Withers, A.C., Médard, E., Laumonier, M., Laporte, D., Flaherty, T., Gómez-Ulla, A., 2018. Water quantification in silicate glasses by Raman spectroscopy: correcting for the effects of confocality, density and ferric iron. Chem. Geol. 483, 312–331.
Schiavi, F., Bolfan-Casanova, N., Buso, R., Laumonier, M., Laporte, D., Medjoubi, K., Venugopal, S., Gomez-Ulla, A., Cluzel, N., Hardiagon, M., 2020. Quantification of magmatic volatiles by Raman microtomography of glass inclusions-hosted bubbles. Geochem. Perspect. Lett. 16, 17–24.
Shcheka, S.S., Wiedenbeck, M., Frost, D.J., Keppler, H., 2006. Carbon solubility in mantle minerals. Earth Planet. Sci. Lett. 245 (3–4), 730–742.
Silver, L., Stolper, E., 1989. Water in albitic glasses. J. Petrol. 30 (3), 667–709.
Skogby, H., 2006. Water in natural mantle minerals I: pyroxenes. In: Keppler, H., Smyth, J.R. (Eds.), Water in Nominally Anhydrous Minerals. De Gruyter, pp. 155–167.
Sokol, A.G., Kupriyanov, I.N., Palyanov, Y.N., 2013. Partitioning of H_2O between olivine and carbonate-silicate melts at 6.3 GPa and 1400°C: implications for kimberlite formation. Earth Planet. Sci. Lett. 383, 58–67.
Stagno, V., Frost, D.J., McCammon, C.A., Mohseni, H., Fei, Y., 2015. The oxygen fugacity at which graphite or diamond forms from carbonate-bearing melts in eclogitic rocks. Contrib. Miner. Petrol. 169 (2), 16.
Stolper, E., 1982. Water in silicate glasses: an infrared spectroscopic study. Contrib. Miner. Petrol. 81 (1), 1–17.
Stracke, A., 2012. Earth's heterogeneous mantle: a product of convection-driven interaction between crust and mantle. Chem. Geol. 330–331, 274–299.
Stracke, A., Hofmann, A.W., Hart, S.R., 2005. FOZO, HIMU, and the rest of the mantle zoo. Geochem. Geophys. Geosyst. 6 (5), Q05007.
Syracuse, E.M., van Keken, P.E., Abers, G.A., 2010. The global range of subduction zone thermal models. Phys. Earth Planet. In. 183 (1–2), 73–90.
Taracsák, Z., Hartley, M.E., Burgess, R., Edmonds, M., Iddon, F., Longpré, M.-A., 2019. High fluxes of deep volatiles from ocean island volcanoes: insights from El Hierro, Canary Islands. Geochim. Cosmochim. Acta 258, 19–36.
Tenner, T.J., Hirschmann, M.M., Withers, A.C., Hervig, R.L., 2009. Hydrogen partitioning between nominally anhydrous upper mantle minerals and melt between 3 and 5 GPa and applications to hydrous peridotite partial melting. Chem. Geol. 262 (1–2), 42–56.
Tenner, T.J., Hirschmann, M.M., Humayun, M., 2012. The effect of H_2O on partial melting of garnet peridotite at 3.5 GPa. Geochem. Geophys. Geosyst. 13 (3), Q03016.
van Gerve, T.D., Neave, D.A., Wieser, P., Lamadrid, H., Hulsbosch, N., Namur, O., 2024. The origin and differentiation of CO_2-rich primary melts in ocean island volcanoes: integrating 3D X-ray tomography with chemical microanalysis of olivine-hosted melt inclusions from Pico (Azores). J. Petrol. 65 (2), 1–24.
Venugopal, S., Schiavi, F., Moune, S., Bolfan-Casanova, N., Druitt, T., Williams-Jones, G., 2020. Melt inclusion vapour bubbles: the hidden reservoir for major and volatile elements. Sci. Rep. 10, 9034.
Willbold, M., Stracke, A., 2010. Formation of enriched mantle components by recycling of upper and lower continental crust. Chem. Geol. 276 (3–4), 188–197.
Woodhead, J.D., 1996. Extreme HIMU in an oceanic setting: the geochemistry of Mangaia Island (Polynesia), and temporal evolution of the Cook—Austral hotspot. J. Volcanol. Geoth. Res. 72 (1–2), 1–19.
Yang, X., Liu, D., Xia, Q., 2014. CO_2-induced small water solubility in olivine and implications for properties of the shallow mantle. Earth Planet. Sci. Lett. 403, 37–47.
Yasuda, A., Fujii, T., Kurita, K., 1994. Melting phase relations of an anhydrous mid-ocean ridge basalt from 3 to 20 GPa: implications for the behavior of subducted oceanic crust in the mantle. J. Geophys. Res. 99 (B5), 9401–9414.